

# **Time-domain diffuse correlation spectroscopy: instrument prototype, preliminary measurements, and theoretical modeling**

by

Danil Tyulmankov

S.B., EECS and BCS, MIT (2016)

Submitted to the Department of Electrical Engineering and Computer Science  
in partial fulfillment of the requirements for the degree of

Master of Engineering in Electrical Engineering and Computer Science

at the

MASSACHUSETTS INSTITUTE OF TECHNOLOGY

February 2017

© 2017 Danil Tyulmankov. All rights reserved.

The author hereby grants to MIT permission to reproduce and to distribute publicly paper  
and electronic copies of this thesis document in whole or in part in any medium now known  
or hereafter created.

Author .....  
Department of Electrical Engineering and Computer Science  
February 3, 2017

Certified by .....  
Maria Angela Franceschini  
Associate Professor of Radiology, Harvard Medical School  
Thesis Supervisor

Certified by .....  
Elfar Adalsteinsson  
Professor of Electrical Engineering and Computer Science, MIT  
Thesis Co-Supervisor

Accepted by .....  
Christopher Terman  
Chairman, Masters of Engineering Thesis Committee



# **Time-domain diffuse correlation spectroscopy: instrument prototype, preliminary measurements, and theoretical modeling**

by

Danil Tyulmankov

Submitted to the Department of Electrical Engineering and Computer Science  
on February 3, 2017, in partial fulfillment of the  
requirements for the degree of  
Master of Engineering in Electrical Engineering and Computer Science

## **Abstract**

Near-infrared spectroscopy (NIRS) is an emerging diffuse optical imaging tool with both clinical and academic applications such as functional brain imaging, breast cancer detection, and cerebral health monitoring. Due to its non-invasiveness, high spatial and temporal resolution, and portability, it has been rapidly growing in popularity over the last 40 years. The technique relies on near-infrared light to measure optical properties – scattering and absorption – which can then be used to infer details of the underlying tissue physiology. Diffuse correlation spectroscopy (DCS) is a complimentary optical technique that relies on long-coherence laser light, also in the near-infrared range, to measure dynamical properties of a medium – in the biomedical context, blood flow. While NIRS and DCS can be used in conjunction to provide even more powerful information, they require separate instrumentation, resulting in reduced portability and difficulty in bedside monitoring. In brain imaging applications, both NIRS and DCS suffer from confounds due to layers surrounding the brain, such as the scalp and skull. While this issue has been addressed in NIRS using time-resolved instrumentation known as time-domain (TD) NIRS, it has been largely ignored in the context of DCS.

In this work, we demonstrate a novel time-domain diffuse correlation spectroscopy (TD-DCS) technique embodied in a single instrument capable of simultaneously measuring optical and dynamical properties. Along with maintaining portability, the instrument reduces error by directly measuring the absorption and scattering values necessary for precise flow estimation, and removes a major confounding factor by suppressing unwanted signal from superficial layers through time-gating. We describe the construction of the first instrument prototype and demonstrate the depth resolution proof-of-concept with measurements of multi-layer media. We further discuss the theoretical considerations of modeling the light interaction with tissue, necessary for reliable estimates.

Thesis Supervisor: Maria Angela Franceschini

Title: Associate Professor of Radiology, Harvard Medical School

Thesis Co-Supervisor: Elfar Adalsteinsson

Title: Professor of Electrical Engineering and Computer Science, MIT



# Preface and Acknowledgments

*“The more we learn about the world, and the deeper our learning, the more conscious, specific, and articulate will be our knowledge of what we do not know, our knowledge of our ignorance.”*

---

Karl Popper (1963)

Despite the incredible amount I have learned in the last two years, I can make no claims about being an expert in this field. Although I now know far more than I did when I first discovered diffuse optics, even more so I have come to realize how much I have yet to learn. It is beyond the scope of this work to describe in detail all that we *do* know about the field, so instead I write this to outline what there *is* to know. A comprehensive yet basic introductory text is difficult to find, so in addition to serving as the capstone of my past two years of learning and research, I write this thesis in hopes that it might be a good first exposure for someone who is just entering the field of biomedical diffuse optics. In other words, I write this for myself, two years ago, and hope it will be useful for someone who finds themselves in a similar situation. For this reason, I exclude most of the mathematical rigor and derivations, providing only the necessary context and intuition to more easily parse the details provided in the references. In addition to the background necessary for my project, I make an attempt to provide a small amount of history, give a bird’s-eye view of the field, and organize the various terminology.

I have many people to thank for helping me get to where I am now. First and foremost, I want to thank Mari for giving me the opportunity to explore a field I knew nothing about, and for her patience, guidance, and unwavering support throughout all of the inevitable ups and downs of this project. I thank David Boas for his insights into the theory behind the techniques discussed in this thesis, and the invaluable feedback on the experiments. Thank you to Jason Sutin for his engineering expertise and meticulous supervision, without whom the construction of the prototype would have been impossible. Of course, thank you to the Optics Division, and the entirety of the MGH/HST Martinos Center, in particular to Bruce Rosen for sharing his wisdom in trying times.

Outside of the Martinos Center, I want to thank Alexander Friedman for his mentorship during my undergraduate years, for pushing me to my maximum potential and beyond, and for preparing me for my graduate work. I thank my academic advisor, Dennis Freeman, for his patience, encouragement, advice, and availability despite increasingly hefty responsibilities. Finally, I thank Anne Hunter, who was the first to welcome me to the EECS department during my transfer from UMass Amherst my freshman year: “I’m not making any promises, but so far everyone whom I have recommended has been accepted.” Without her, I am convinced, Course 6 would have long ago collapsed into anarchy.



# Contents

Abstract . . . . .	3
Preface and Acknowledgments . . . . .	5
<b>1 Introduction and Background</b>	<b>9</b>
1.1 Near-Infrared Spectroscopy (NIRS) . . . . .	11
1.1.1 Fundamentals: Light and Physiology . . . . .	14
1.1.2 Continuous Wave (CW-NIRS) . . . . .	21
1.1.3 Frequency Domain (FD-NIRS) . . . . .	24
1.1.4 Time Domain (TD-NIRS) . . . . .	24
1.2 Measurement using coherent light . . . . .	29
1.2.1 Fundamentals: Interference and Coherence . . . . .	29
1.2.2 Dynamic Light Scattering (DLS) . . . . .	33
1.2.3 Diffusing Wave Spectroscopy (DWS) . . . . .	39
1.2.4 Diffuse Correlation Spectroscopy (CW-DCS) . . . . .	42
1.2.5 Time-Domain Diffuse Correlation Spectroscopy (TD-DCS) . . . . .	46
<b>2 Completed Work</b>	<b>49</b>
2.1 Instrument prototype construction . . . . .	49
2.2 Data analysis methods . . . . .	54
2.2.1 Computing the temporal point spread function . . . . .	54
2.2.2 Estimating $\mu_a$ and $\mu'_s$ . . . . .	56
2.2.3 Computing the autocorrelation function . . . . .	57
2.2.4 Estimating $\beta$ and BFi . . . . .	62
2.2.5 Time-gating the photons . . . . .	63
2.3 Results . . . . .	65
2.3.1 Initial measurements . . . . .	65
2.3.2 Two-layer phantom . . . . .	66
2.3.3 Measured vs. theoretical values of $\beta$ . . . . .	68
2.4 Conclusions and further work . . . . .	73
<b>A Code library</b>	<b>78</b>
A.1 times_to_bins.m . . . . .	78
A.2 acorr_times.m . . . . .	79
A.3 rebin_to_multitau.m . . . . .	79
A.4 dcs_fit.m . . . . .	80
A.5 g2_seminf.m . . . . .	81

A.6	fold_tpsf.m . . . . .	82
A.7	fold_micro.m . . . . .	83
A.8	g2_sim.m . . . . .	84
A.9	tps_sim.m . . . . .	85



# Chapter 1

## Introduction and Background

Since the late 19th century, when Santiago Ramón y Cajal established the neuron doctrine – the groundbreaking idea that the brain is made up of individual cells – the field of neuroscience has grown at a rapid rate. Numerous techniques for monitoring the brain in both academic and clinical settings have been developed. Electroencephalography (EEG) or magnetoencephalography (MEG), for example, records the electric or magnetic fields resulting from activity of large groups of neurons. Functional magnetic resonance imaging (fMRI), measures a correlate of neural activity caused by the presence of oxygenated blood in the working area of the brain. The ideal neuroimaging technology would be portable, non-invasive, and have both high spatial and temporal resolution (Fig. 1.1). Diffuse optics, a field expanding at an exponential [1] rate, provides us with the potential to meet many of these requirements.

Near-infrared spectroscopy (NIRS), as the name implies, uses near-infrared light to measure optical properties of a medium – absorption and scattering. Given these optical properties, we can then infer the physical properties such as chromophore concentration, or even make spatial maps of the inhomogeneities present in the medium. In the neuroimaging context, this allows us to localize blood oxy- and deoxy-hemoglobin concentrations and thus

quantify functional activity in the brain [1, 2]. In the clinical setting it can be used for diagnostics such as breast cancer, heart disease, muscle pathophysiology, and many others [3].

Diffuse correlation spectroscopy (DCS) is a complementary technique that takes advantage of the coherence of light to measure dynamical<sup>1</sup> properties of a medium such as blood flow in tissue [4, 5]. Conditions such as cardiovascular disease, stroke, head trauma, peripheral arterial disease, and cancer can be related to abnormal blood flow, and thus DCS can provide information for disease diagnostics and treatment efficacy metrics.

The combination of these techniques provides us with even more powerful information. In particular, we need to know the optical properties to estimate dynamical properties. Using NIRS concurrently with DCS gives us directly measured optical properties in the subject, without having to resort to tabulated average values. Furthermore, if we combine DCS blood flow data with NIRS measurements of hemoglobin concentrations, we can then calculate the cerebral metabolic rate of oxygen consumption, which is a reliable measure of brain health [6, 7].

In the neuromonitoring setting, however, both NIRS and DCS suffer from confounding effects of the layers surrounding the brain such as the skull and the scalp. It has been demonstrated that using time-domain techniques for near-infrared spectroscopy improves the measurement’s sensitivity to the brain [9]. In this work we explore how time-domain NIRS can be extended to DCS with the introduction of a novel technique termed *time-domain diffuse correlation spectroscopy* (TD-DCS).

We begin Chapter 1 with a thorough summary of the developments in the field of diffuse optics. We introduce the physical principles of making measurements with near-infrared light

---

<sup>1</sup>A note on language: it may be tempting to say “static” absorption and scattering properties in contrast with “dynamic” flow properties. In fact, absorption and scattering properties may vary with time (for example, as a result of changes in chromophore concentrations – functional NIRS [1, 2] takes advantage of this phenomenon to measure brain activity), so we refer to them as *optical* properties to differentiate them from *dynamical* (not “dynamic”) flow properties

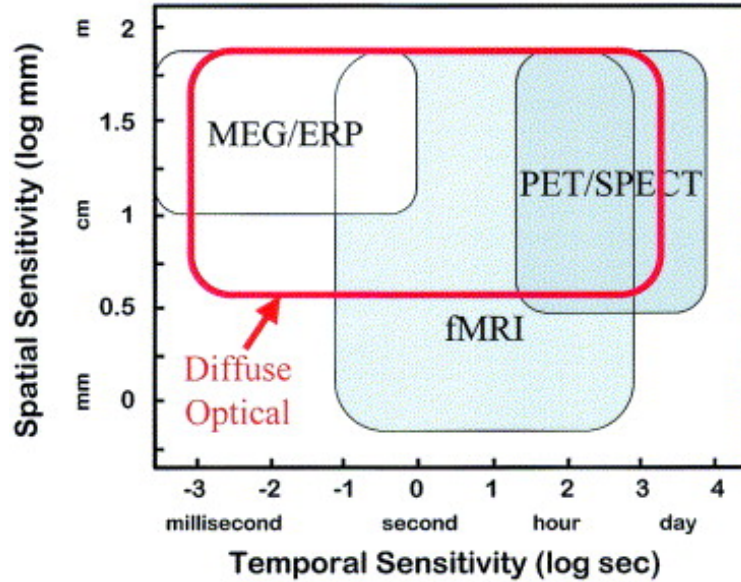


Figure 1.1: Comparison of spatial and temporal resolution of various neuroimaging techniques. Reprinted from [8], with permission from Elsevier

as well as the experimental setup and analysis techniques used in the various implementations of this principle. The focus is on developing the concepts leveraged by TD-DCS. In Chapter 2, we outline the construction of the first prototype TD-DCS system and demonstrate proof-of-principle with measurements on artificial phantoms. We also explore the impact of coherence length on the measured DCS correlation function in the time domain. Understanding this is critical for the development of the right model for the TD-DCS correlation function to accurately estimate flow.

## 1.1 Near-Infrared Spectroscopy (NIRS)

To set the ground for understanding the “time-domain” ideas behind time-domain diffuse correlation spectroscopy, we begin with a discussion of a related optical imaging technique known as near-infrared spectroscopy (NIRS). We discuss three of its variations – continuous-

wave, frequency-domain, and time-domain<sup>1</sup>. As the name implies, the third lays the foundation for the “time-domain” aspects of TD-DCS.

There is a multitude of spectroscopic techniques that rely on the scattering and absorption of light, with experimental work dating as early as the 19<sup>th</sup> century. Biomedical applications using near-infrared (NIR) light, however, were limited to superficial layers of tissue until 1977, when Frans Jöbsis discovered that it could also be used to probe thicker samples. He used NIRS to measure in vivo brain hemodynamics [12], thus spurring the recent 40 years of development in this field. (See [13] for a more detailed account on the history of NIRS). In contrast to prior approaches, NIRS measures *diffuse* light that has scattered many times and an individual photon trajectory is a random walk, so in bulk they are estimated by a diffusion equation. Thus, this technique is also often referred to as diffuse optical spectroscopy (DOS).

The fundamental idea behind NIRS is quite straightforward: we shine light into the tissue, measure it after it passes through, and then use an appropriate model to interpret the difference between the incident and detected light. NIRS is typically divided into three categories based on the type of incident light used and on what is measured by the detector. See Fig. 1.2 for an illustration of these ideas. First, the most simple and inexpensive continuous-wave (CW) systems illuminate the tissue with a *constant-amplitude continuous* light and simply use the light's attenuation to measure absorption. Next, frequency-domain (FD) systems use *amplitude-modulated continuous* light and measure not only attenuation but also phase shift (delay) to get information about both absorption and scattering properties. Finally, time-domain (TD) systems use extremely short (on the order of a few picoseconds) *pulses* of light and measure the time-of-flight of individual photons to determine not only absorption and scattering but also the pathlength of the photon to provide depth resolution.

Independent of the type of incident light used, one can also set up various configura-

---

<sup>1</sup>In fact, frequency-domain and time-domain NIRS carry the same type of information, so in some literature they are together referred to as “time-resolved spectroscopy” (TRS) [10]. Other authors reserve the term TRS solely for time-domain NIRS [11].

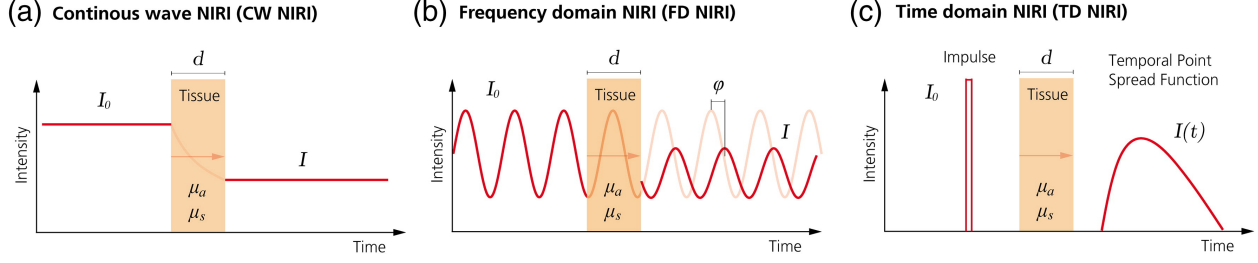


Figure 1.2: Comparison of the three variants of NIRS, illustrating the type of light used to probe the tissue. Reprinted from [10], with permission from Elsevier.

tions of light sources and detectors to measure optical properties as a function of location. In principle, NIRS or DOS strictly refers to a point-measurement instrument with a single source location and one (or more) detectors. In contrast, diffuse optical imaging (DOI) [8], otherwise referred to as near-infrared imaging (NIRI) or topography, [10] uses multiple source-detector pairs, or a single one used to measure multiple locations [14, ch. 9.1.4], to reconstruct 2D images of the tissue using optical properties as contrast. Finally, diffuse optical tomography (DOT) requires spatially overlapping measurements from multiple sources for 3D reconstructions [15, ch. 2.4.2]. We use the NIRS terminology to distinguish these techniques from diffuse correlation spectroscopy (DCS), described in §1.2.4.

Additionally, for a given source-detector pair, we can also vary their placement relative to the measured medium. In the *transmission* (or, *transmittance*) geometry, the source and detector are placed on opposite surfaces, with the measured medium in the middle (Fig. 1.3a). In the *reflectance* (or, *backscattering*) geometry, we place source and detector on the same surface, separated by a few centimeters (Fig. 1.3b). Since in many biomedical applications the samples such as the human head are too thick or opaque, we cannot measure the light passing through the medium in the transmittance geometry. In this case, we take advantage of the fact that tissue is highly scattering and light diffuses in all directions, therefore illuminating a detector arranged in the reflectance geometry.

We limit the discussion here to the basics of NIRS, and the concepts necessary for the

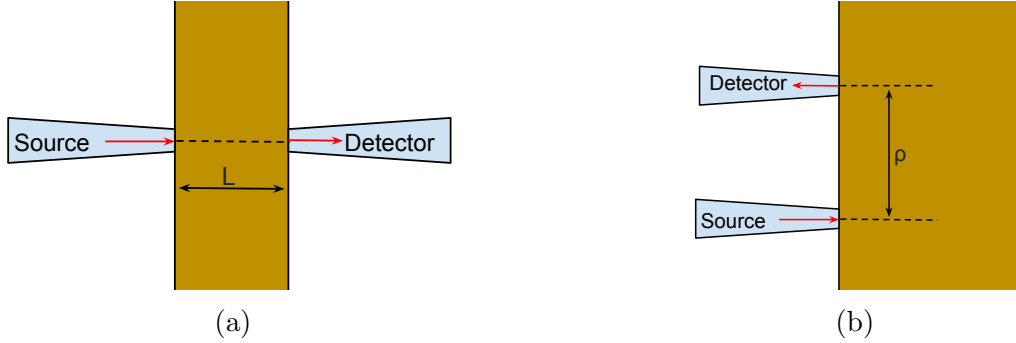


Figure 1.3: (a) Transmission geometry through an infinite homogeneous slab of thickness  $L$ . (b) Reflectance geometry in a semi-infinite homogeneous medium with a source-detector separation  $\rho$ .

development of the theory behind TD-DCS. The focus will be point-measurements, as the image reconstruction algorithms [16] are beyond the scope of this work. There are also variations of each of these techniques, such as spatially resolved spectroscopy (SRS) [11], [15, ch. 2.4.2] which uses multiple source-detector separations for a point-measurement to get better estimates, or broadband diffuse optical spectroscopic imaging which uses the entire spectrum of light for measurements [14, ch. 9]. The details of the many applications of the technique and interpretations of the data are also omitted. Finally, we mention that there exist many other biomedical optical techniques that take advantage the same scattering and absorption phenomena, although for different applications and go by different names such as reflectance spectroscopy [14, ch. 6] or light scattering spectroscopy [14, ch. 8].

### 1.1.1 Fundamentals: Light and Physiology

Before we begin the more detailed discussion of NIRS, we present the fundamental concepts about light that are central to the techniques presented here, as well as some facts about its interaction with tissue.

## Light, Absorption, and Scattering

It is well-known that light is an electromagnetic wave, the simplest of which is a monochromatic plane wave. For simplicity we ignore the spatial extent and polarization, and suffice with a one-dimensional scalar description given by

$$E(x, t) = E_0 \cos(kx - \omega t + \phi) = \text{Re}\{E_0 e^{i(kx - \omega t + \phi)}\} = \text{Re}\{\tilde{E}(x, t)\} \quad (1.1)$$

The second equality is given by using Euler's formula, where  $\text{Re}\{\cdot\}$  represents the real part. Normally, it is omitted from the notation is always understood to be implicit, so we simply refer to an electromagnetic wave by

$$\tilde{E}(x, t) = E_0 e^{i(kx - \omega t + \phi)} \quad (1.2)$$

In general, however, we cannot directly measure the electromagnetic field. Rather, all optical detectors, including our eyes, can only measure intensity, i.e. the average energy per unit area per unit time, which is related to the electric field by

$$I(x) = \frac{\langle |E(x, t)|^2 \rangle}{\eta} = \frac{\langle |\tilde{E}(x, t)|^2 \rangle}{2\eta} = \frac{\langle \tilde{E}(x, t) \tilde{E}^*(x, t) \rangle}{2\eta} = \frac{E_0^2}{2\eta} \quad (1.3)$$

where  $\eta = \sqrt{\mu/\epsilon}$  is the impedance (a constant resulting from the electric and magnetic properties of the medium),  $E^*$  represents the complex conjugate and  $\langle \cdots \rangle$  represents the time-average

$$\langle f \rangle = \lim_{T \rightarrow \infty} \frac{1}{T} \int_{-T/2}^{T/2} f(t) dt \quad (1.4)$$

Electromagnetic radiation, of course, has another well-known interpretation in terms of quantized particles called photons that when analyzed in bulk appear as an electromagnetic

wave. So the monochromatic wave above can be interpreted as a stream of photons all of which have the same energy, frequency, momentum, and direction.

When light impinges onto matter, it will either be absorbed or scattered. If a photon's energy matches the difference in energy levels of an atom, the photon will be absorbed and its energy will be dissipated, e.g. as heat. In bulk matter, this phenomenon can be quantified using the Beer-Lambert Law (otherwise called Beer-Lambert-Bouguer Law or simply Beer's Law):

$$I(\lambda) = I_0(\lambda)e^{-\mu_a(\lambda)\rho} \quad (1.5)$$

or in its canonical form:

$$A(\lambda) \equiv -\log \frac{I(\lambda)}{I_0(\lambda)} = \mu_a(\lambda)\rho \quad (1.6)$$

where  $I_0$  is the intensity of the light from the source,  $I$  is the measured light intensity at the detector,  $\rho$  is the source-detector separation, and  $\mu_a(\lambda)$  is the absorption coefficient, which depends on the properties of the medium. The quantity  $-\log \frac{I}{I_0}$  is defined as the optical density (OD) or attenuation<sup>1</sup> (A). The law states that as light passes through the medium over a longer distance, the intensity drops exponentially. In a solution, the absorption coefficient is proportional to the concentrations of *chromophores* (light-absorbing compounds)

$$\mu_a(\lambda) = \sum_i c_i \varepsilon_i(\lambda) \quad (1.7)$$

where  $c_i$  is the concentration of chromophore  $i$  and  $\varepsilon_i(\lambda)$  is the proportionality factor called the *extinction coefficient* [14, ch. 8.2.1]. Thus, the attenuation of a medium is proportional to both the distance the light travels, as well as the chromophore concentration. Note that this relation is explicitly written as a function of  $\lambda$  (omitted henceforth for brevity) – it is wavelength-dependent, since the extinction coefficient varies for different wavelengths. This

---

<sup>1</sup>Also note the related quantity transmittance is defined as  $T \equiv \frac{I}{I_0}$



relation only holds if the medium is non-scattering, the chromophores are independent of each other, and the concentration is homogeneous along the light path. [15, ch. 2]

If a photon's energy is not high enough to cause a transition to a higher energy state, the atom's electron cloud is nevertheless driven into oscillation. As an oscillating electric dipole, the atom will immediately re-radiate the photon with the same amount of energy and wavelength, in a random direction. This is known as elastic scattering and will be the primary scattering mechanism at work in our discussion. As scattering depends not only on the individual atoms but also on the structure of the molecule, as well as the spacing and interactions of molecules in the medium, there are multiple models of scattering applicable for different scenarios. Rayleigh scattering describes independent particles smaller than a wavelength of light arranged randomly in space. Mie scattering deals with particles larger than a wavelength. Inelastic scattering, in contrast, does not preserve the wavelength of the photon. Raman scattering is an example of this phenomenon.

## **Tissue optical properties**

Light is absorbed and scattered by matter, and human tissue is no exception. Although we may seem opaque to visible light at first glance, a simple demonstration will indicate otherwise. If one covers a bright flashlight with his hand, the tissue will faintly glow red. As the incident light from the flashlight is white and contains all visible wavelengths, we see that red (and, in fact, infrared) light is least absorbed by tissue. We also see that the light exiting the tissue no longer resembles the rays of the incident light as it has also been scattered many times and is considered *diffuse*. As we discuss in the next section, the photons can therefore be modeled as undergoing a diffusion process through the medium.

The primary optical absorbers (chromophores) in tissue include water, lipid, melanin, and hemoglobin. As shown in Fig. 1.4, in biologically relevant conditions, the absorption

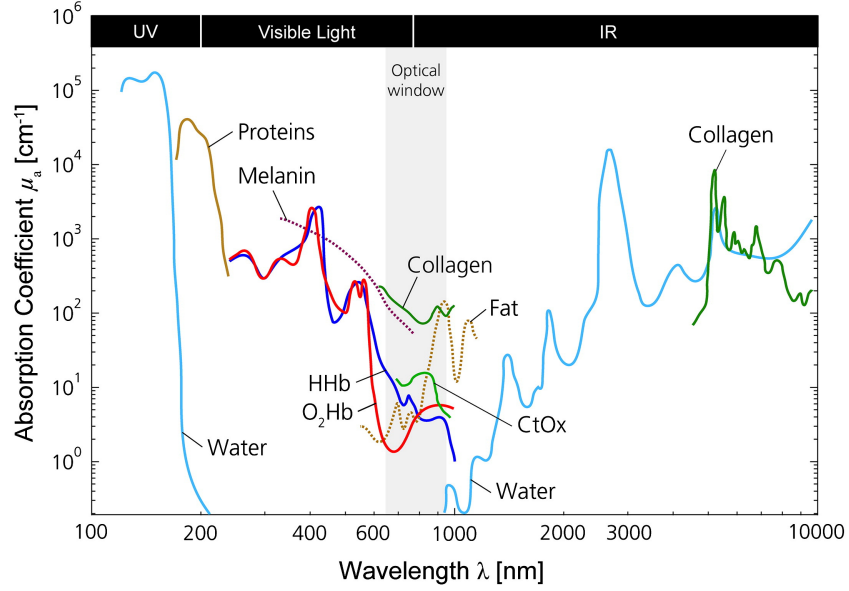


Figure 1.4: Absorption spectra of various biological chromophores at concentrations typically seen in tissue. Reprinted from [10], with permission from Elsevier.

is lowest in the near-infrared range ( $\sim 600\text{-}900\text{nm}$ ), also called the *optical window*, allowing us to use light of these frequencies to investigate biological tissue. The parameter that describes the absorption of a material, as mentioned above, is  $\mu_a$ , the absorption coefficient. It is defined as the inverse of the average distance a photon travels in the medium before being absorbed (i.e.  $\mu_a \equiv \frac{1}{l_a}$  where  $l_a$  is the expected path length before encountering an absorber), typically given in units of  $[\text{cm}^{-1}]$ .

Elastic (Rayleigh and Mie) scattering is the source of the diffusive nature of light in tissue. The primary static scatterers include connective tissue, collagen, skin, as well as cellular organelles. Dynamic scattering is caused primarily by the movement of red blood cells and will be the focus of the discussion in §1.2. It is typically ignored in the context of NIRS. The scattering coefficient  $\mu_s$  summarizes the scattering properties of the material, and is defined analogously to  $\mu_a$  as the inverse of the average distance a photon travels before being scattered (i.e.  $\mu_s \equiv \frac{1}{l_s}$  where  $l_s$  is the *mean free path*), also typically presented in  $[\text{cm}^{-1}]$ . Scattering, however, is often not equally likely in all directions, i.e. it is not isotropic.

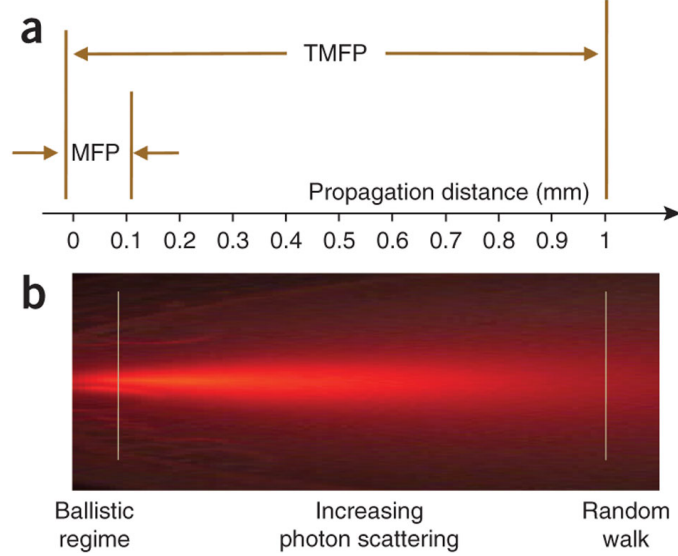


Figure 1.5: (a) Schematic illustration of the mean free path (MFP)  $l_s = \frac{1}{\mu_s}$  and transport mean free path (TMFP)  $l^* = \frac{1}{\mu'_s}$ . (b) Corresponding photon distribution during light propagation for  $\mu'_s = 10\text{cm}^{-1}$ . Reprinted from [17] with permission from Nature Publishing Group.

Thus we introduce the anisotropy factor  $g \equiv \langle \cos \theta \rangle$  (ranging from -1 to 1) as the average of the cosine of the scattering angle. For isotropic (Rayleigh) scattering,  $g = 0$ ; for total forward scattering (Mie scattering at large particles),  $g = 1$ ; for total backward scattering,  $g = -1$  [14, ch. 5.2]. The reduced scattering coefficient  $\mu'_s$  is then defined as  $\mu'_s \equiv \mu_s(1 - g)$  (and similarly we have  $\mu'_s \equiv \frac{1}{l^*}$  where  $l^*$  is the *transport mean free path*). See Fig. 1.5 for an illustration of the photon scattering behavior over these length scales.

## Modeling light transport

To fully understand the interaction of light with matter, we would like to create a model of its propagation through the medium. Given measurements of light, inverting the model would then allow us to make inferences about the medium.

One option is to run a Monte Carlo simulation. Given a three-dimensional model of the medium with known optical properties, we simulate the propagation of individual photons

through the medium, using the scattering and absorption properties to probabilistically generate their trajectories, and record those that reach the detector [18]. It is considered the “gold standard” for modeling, as it is valid for arbitrary three-dimensional configurations of tissue properties and source-detector positioning. The primary limitation of this method, however, is computational. To achieve statistically significant results, we must keep track of the trajectories of several million individual photons and so a single Monte Carlo simulation can take as long as several hours or even days.

The alternative is to create a mathematical model of the light propagation in tissue. Light transport is described with the radiative transport equation (RTE), otherwise known as the Boltzmann equation, which describes the spatial and temporal distribution of radiance  $L(r, t, \hat{s})$  in a volume:

$$\begin{aligned} \frac{1}{c} \frac{\partial L(r, t, \hat{s})}{\partial t} + \hat{s} \cdot \nabla L(r, t, \hat{s}) + (\mu_a + \mu_s) L(r, t, \hat{s}) \\ = \mu_s \int_{4\pi} L(r, t, \hat{s}') P(\hat{s}, \hat{s}') d\Omega + S(r, t, \hat{s}) \end{aligned} \quad (1.8)$$

In the case where  $\mu_s \gg \mu_a$ , i.e. there are many more scattering than absorption events as is typical in turbid samples such as biological tissue, we can approximate the radiative transport equation with the diffusion equation, describing the steady-state diffusion of the fluence rate  $\Phi(r, t)$  through a volume:

$$\left( -\frac{1}{3(\mu_a + \mu'_s)} \nabla^2 + \mu_a \right) \Phi(r, t) = S_0(r, t) \quad (1.9)$$

For details and a derivation, see [15, ch. 3]. The diffusion equation can then be solved to get a closed form for  $\Phi(r, t)$  for different source types (e.g. CW, FD, TD) and tissue geometries (e.g. infinite, semi-infinite, slab) [19, 20, 21, 22]. For example, for a steady-state (i.e. CW) source in a semi-infinite homogeneous medium, with a reflection geometry with

source-detector separation  $\rho$  (Fig. 1.3b) we can show that the fluence rate is given by

$$\Phi_{CW}(t) = \frac{vS_0}{4\pi D} \left[ \frac{e^{-kr_1}}{r_1} - \frac{e^{-kr_2}}{r_2} \right] \quad (1.10)$$

where  $v$  is the speed of light in the medium,  $S$  is the source intensity, and

$$k = \sqrt{3\mu_a\mu'_s} \quad (1.11) \quad D = \frac{v}{3\mu'_s} \quad (1.14)$$

$$r_1 = \sqrt{\rho^2 + z_0^2} \quad (1.12) \quad z_0 = \frac{1}{\mu'_s} \quad (1.15)$$

$$r_2 = \sqrt{\rho^2 + (z_0 + 2z_b)^2} \quad (1.13) \quad z_b = \frac{2}{3\mu'_s} \frac{1 + R_{\text{eff}}}{1 - R_{\text{eff}}} \quad (1.16)$$

where  $\rho$  is the source detector separation.  $R_{\text{eff}}$  is the effective reflection coefficient and depends on the relative refractive index. It is approximately equal to 0.493 for a refractive index of  $n = 1.4$ . For a discussion of these parameters, see [20] and references therein.

To summarize, the main underlying principle of NIRS is to measure the optical properties of the medium. Then, given models of the underlying physiology and its interaction with light, we can and make estimates about the tissue such as chromophore concentrations.

### 1.1.2 Continuous Wave (CW-NIRS)

Continuous-wave infrared spectroscopy is the simplest of the three methods, and also the cheapest to implement due to the relatively basic instrumentation necessary [10]. While imaging and tomographic arrangements are now in use, along with multiplexing each channel with multiple wavelengths or even broadband (i.e. containing an entire continuous section of the spectrum) light, we describe the most basic implementation of CW-NIRS.

A single source with two wavelengths (e.g. 690 and 830nm for measuring oxygenated and de-oxygenated hemoglobin) of light is used, typically from a pair of lasers or light emitting

diodes (LEDs) delivered to the tissue through an optical fiber. Wavelengths are chosen to minimize cross-talk between chromophores as required by the Beer-Lambert Law (Eq. 1.5). A single detector is used, typically in the form of a photomultiplier tube (PMT), a photodiode, or an avalanche photodiode (APD), and light is collected from the tissue and delivered to the detector through a second optical fiber. We then use the values of the incident and detected intensities for both wavelengths to calculate the concentrations of chromophores of interest – typically, oxygenated and de-oxygenated hemoglobin.

If human tissue did not scatter light, we would be able to then use the Beer-Lambert Law (Eq. 1.5) to easily calculate  $\mu_a$ . Measurements of the light intensity for several different wavelengths (one for each chromophore), would allow us to set up a system of equations to solve for the concentration of each chromophore using Eq. 1.7 (extinction coefficients  $\varepsilon$  have been tabulated for many compounds over many wavelengths) [15, ch. 2], [14, ch. 5]. The reality is, however, that the scattering coefficient  $\mu_s$  is several orders of magnitude larger than the absorption coefficient  $\mu_a$ , violating the premise of the Beer-Lambert law that the medium is non-scattering, so the theory needs to be modified accordingly. Delpy et. al. in 1988 proposed the modified Beer-Lambert Law (MBLL) as follows [23]:

$$A \equiv -\log \frac{I}{I_0} = \mu_a \langle \rho \rangle + G \quad (1.17)$$

where  $\langle \rho \rangle = B\rho$  is the mean optical pathlength, and  $B$  is called the differential pathlength factor (DPF) that accounts for the increased travel distance of a photon due to scattering. The geometry factor  $G$  accounts for losses due to scattering and the measurement geometry.

The geometry factor  $G$  is typically unknown and without it we cannot calculate the absolute concentrations of chromophores. If we assume it is constant, however, we can measure the *change* in concentrations by taking a baseline intensity measurement at time  $t_1$

and a second one at  $t_2$ :

$$\Delta A = A_{t_2} - A_{t_1} \quad (1.18)$$

Substituting Eq. 1.17, we get

$$\Delta A = -\log \frac{I_{t_2}}{I_{t_1}} = \Delta \mu_a B \rho \quad (1.19)$$

where the change in  $\mu_a$  is due only to change in chromophore concentrations, as the extinction coefficient  $\varepsilon$  is a constant property of the chromophore itself.

If we suffice with measuring the changes in chromophore concentrations, we no longer need to calculate  $G$ , but the differential path factor  $B$  remains a problem. Based on the diffusion approximation, we can show theoretically that, for example, in a semi-infinite homogeneous medium the DPF is given by [10]

$$B = \frac{1}{2} \left( \frac{3\mu'_s}{\mu_a} \right)^{\frac{1}{2}} \left[ 1 - \frac{1}{\sqrt{1 + \rho \cdot 3\mu_a\mu'_s}} \right] \quad (1.20)$$

This equation shows that the DPF depends on both the scattering and absorption coefficients, as well as the source-detector separation. In practice, however, it is measured empirically and assumed to be constant over time and location. Like the extinction coefficient, this value is typically tabulated and simply included in the calculation as a constant. The tabulated values themselves are measured using time-domain [24, 23] or frequency-domain [25] techniques. There are also other methods to estimate the DPF using CW light, by either making measurements using a spectrum of light rather than a set of single frequencies (known as broadband DOS), or making measurements at multiple source-detector separations (known as spatially resolved spectroscopy [15, ch. 2.4.2]). These variations are further described in [26].

The primary limitation of CW-NIRS, however, is that the measured drop in intensity

can be attributed to either light absorption by the tissue, or light scattering. Generally, it is due to both and we cannot separate the two effects without making an assumption about the measured medium. This issue can be addressed by measuring the change in phase of light in addition to amplitude, using frequency- or time-domain techniques.

### 1.1.3 Frequency Domain (FD-NIRS)

The detailed principles of frequency-domain NIRS are not relevant for developing the theoretical description of TD-DCS, and so the discussion will be very brief, included only for completeness.

In exchange for more complicated instrumentation, FD-NIRS allows us to make exact measurements of the differential pathlength factor (DPF), avoiding the errors inherent in the estimated values used for CW-NIRS. The source intensity is modulated at radio frequency (on the order of 100MHz), such that the modulation period is shorter than the photon time of flight through the tissue. The phase shift, average intensity, and intensity oscillation of the light is measured after passing through the medium. The phase shift is then proportional to the propagation distance, providing us with a direct measurement of the DPF [15, ch. 2], [14, ch. 19] [26]. Furthermore, given analytical solutions to the light propagating through tissue, [21, 27], we can estimate the optical properties of the medium [25]. Due to the intensity modulation inherent in this technique, the light propagation model is also referred to in the literature as diffusing photon density waves (DPDW) [16, 27, 28].

### 1.1.4 Time Domain (TD-NIRS)

Time-domain near-infrared spectroscopy is a method that is equivalent to FD-NIRS in the information about tissue that it provides, though differing in the measurement principles and instrumentation, and analysis techniques. In theory, the two are related through the Fourier



transform. As with CW- and FD-NIRS, there is a multitude of variations that have been implemented, so we will only describe the methodology in general terms. A more detailed review can be found in [29] or [14, ch. 20].

In TD-NIRS, instead of using a source light that continuously illuminates the tissue, we use a short laser pulse, typically on the order of 10-100ps or less. As a result of its scattering properties, the photons then diffusely propagate through the tissue, some of them taking direct paths from the source to the detector, others traveling deeper into the tissue. Some never reach the detector due to absorption. As a result, when the pulse exits the tissue, it is delayed, attenuated, and broadened, typically several nanoseconds in temporal “width.” The degree to which the pulse is affected by the tissue can then inform us about its optical properties, or the differential path factor discussed in §1.1.2.

As suggested by Delpy et. al. [23], the measured intensity profile of the pulse when it is detected is called the temporal point spread function (TPSF), since we are inputting a temporal “point” (i.e. the input laser pulse is modeled as a delta function) and are measuring how it gets spread out as a function of time. In other words, the TPSF can be considered to be the impulse response of the medium<sup>1</sup>.

One might assume that the photons which arrive at the detector later and therefore a longer pathlength have traveled deeper into the medium; those with a short path remain in the superficial layers. Thus, for a multi-layered medium such as the human head (Fig. 1.6), if we can measure the changes in intensity of only the late photons by “time-gating” only the ones arriving within a specified period, we can measure the changes in optical properties of the deeper layers, reducing the unwanted contributions of the superficial layers.

One implementation of such a time-gated system was constructed in 2005 by Selb et. al.

---

<sup>1</sup>It is worth noting that the measured TPSF is actually a convolution of the laser pulse with the “true” TPSF and the impulse response function of the detector system, so it may be necessary to remove the effects of the measurement system before analyzing the TPSF. In practice, since the pulses are of negligible width compared to the width of the tissue TPSF, this can be ignored [14, ch. 20.4.1].

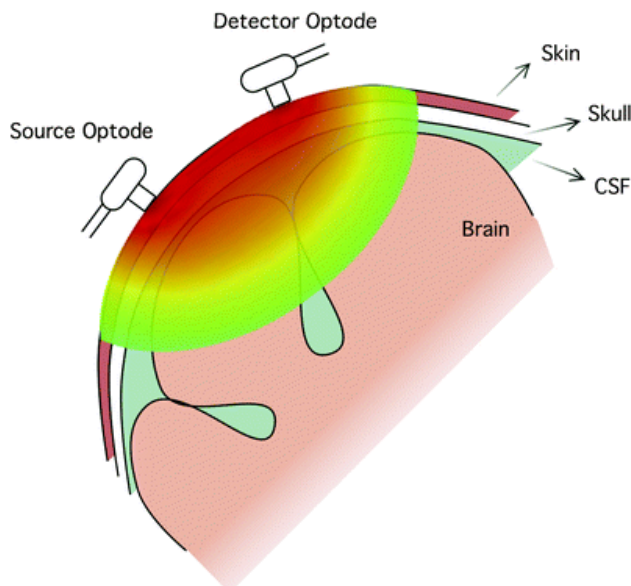


Figure 1.6: Illustration of a typical measurement of the brain using diffuse light. The measured volume is highlighted. Note that it includes layers of tissue that confound the measurement of the brain. Also note that the semi-infinite slab geometry that is typically used to model this setup is only an approximation of the curvature of the head. Reprinted from [15, ch. 3], with permission from Springer.

[9]: the investigators used a fast electronically shuttered detector to measure the intensity during 500ps temporal gate at seven different time delays. For example, opening the shutter for 500ps with no delay measures the average intensity during the first 500ps of the TPSF. Delaying the shutter by 500ps measures the intensity in the next 500ps time block, and so forth. An analysis using the modified Beer-Lambert law similar to the one described in §1.1.2 can then be used to infer changes in optical properties at varying depths, with early blocks corresponding to superficial layers and late blocks to deeper ones. Furthermore, the resulting measurements can be used to reconstruct the TPSF since we have a sample of the intensity at different points in the TPSF.

The more popular approach to measuring the TPSF is by a technique known as time-correlated single photon counting (TCSPC). In practice, the TPSF cannot be recorded all at once from a single pulse of light. Rather, the medium is illuminated with a train of pulses at

a repetition rate on the order of 100MHz. Due to the low average power of the light, at most one photon then reaches the detector for every pulse (rather, this is an assumption made since it's impossible to guarantee due to the probabilistic nature of photon arrivals). In this setup, the only detector that is sensitive enough is either a photomultiplier tube (PMT) or single-photon avalanche photodiode (SPAD). The computer then records the time-of-flight of the photon (i.e. the length of time between the input laser pulse and the arrival of the photon) and records it in a histogram. This histogramming process is repeated until a sufficient number of photons have been accumulated to reconstruct the shape of the TPSF from the histogram. The critical principle here is that there is a greater flux of photons whenever the intensity is higher, so a photon with a time-of-flight that corresponds to the TPSF peak is far more likely to reach the detector than one with a time-of-flight corresponding to the far end of the tail. This concept is illustrated in Fig. 1.7. A more in-depth summary of TCSPC systems can be found in [30], and a detailed account of methods and applications in [31, 32].

The TPSF can be used to determine the absolute tissue optical properties. We first derive the theoretical model of light transport for a pulse of light in terms of the optical properties using the diffusion equation as first suggested by Patterson et. al. in 1989 [19]. This gives us a prediction of the light intensity as a function of time, i.e. the TPSF. For example, for a semi-infinite medium and a reflectance geometry with a source-detector separation of  $\rho$ , the theoretical TPSF is given by [22]

$$\Phi_{TD}(t) = \frac{vS}{(4\pi Dt)^{3/2}} \left[ \exp\left(-\frac{r_1^2}{4Dt}\right) - \exp\left(-\frac{r_2^2}{4Dt}\right) \right] \exp(-v\mu_a t) \quad (1.21)$$

where the variables are the same as in Eq. 1.10. This solution is obtained from Eq. 1.9 using the appropriate boundary conditions, and an impulse source (in contrast to the steady-state source used to obtain Eq. 1.10).

Given the measured TPSF, we can use a fitting algorithm that tunes the relevant param-

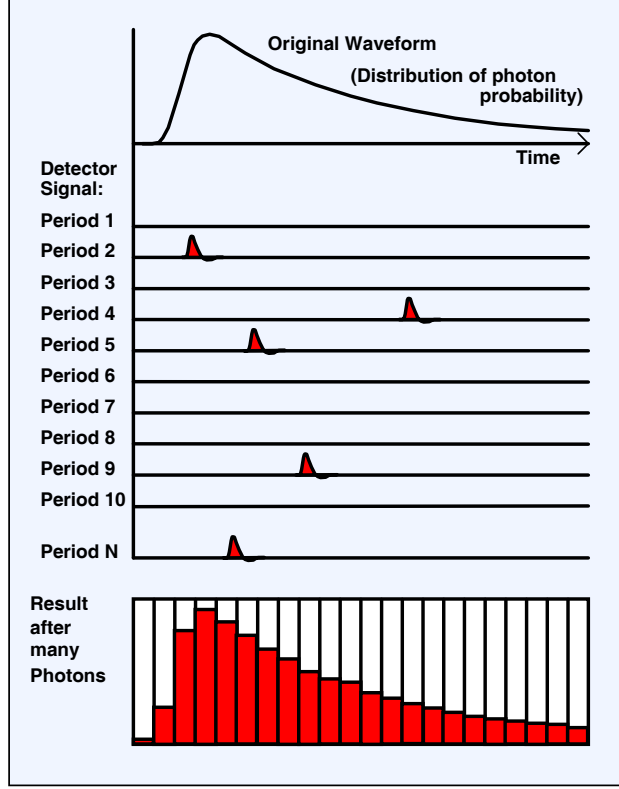


Figure 1.7: Conceptual illustration of time-correlated single photon counting, see text for details. Reprinted from [32].

eters,  $\mu_a$  and  $\mu'_s$  (recall that  $m\mu'_s$  is part of the photon diffusion coefficient  $D$ ) until we achieve the optimal agreement between the measurement and the theory. Note that the histogram amplitude depends on the measurement time, so it must be normalized for fitting. Of course, this requires the assumption that the conditions used in the theoretical derivation match the ones used in the measurement. For example, in Eq. 1.21, we calculate the TPSF for a reflection geometry with a medium that is assumed to extend infinitely away from the light source as in Fig. 1.3b. In practice, our measurement setup more closely resembles Fig. 1.6. This means when performing the measurement the tissue volume must be large enough that the boundary effects of the far edges can be neglected. Clearly, it is also assumed that photon propagation through the medium can be modeled as a diffusion process, that is  $\mu'_s \gg \mu_a$ .

## 1.2 Measurement using coherent light

Note that for NIRS (§1.1) we only rely on measurements of the average intensity of light, and make no implications about its coherence properties. As such, we use those methods to measure optical properties of the medium such as absorption and scattering. In contrast, in this section we use the coherence of light as a metric for dynamical properties of the medium such as flow and Brownian motion.

### 1.2.1 Fundamentals: Interference and Coherence

As in the previous section, we begin with a brief discussion of the basic concepts which are the workhorse of the spectroscopic techniques discussed in this section.

#### Interference

As a thought experiment, consider two monochromatic waves  $E_1$  and  $E_2$  (Eq. 1.2) of the same wavelength traveling along the same axis and impinging on a screen located at position  $x$  where their intensity can be measured (as will be discussed shortly, this is an idealization and truly monochromatic waves cannot exist, but it illustrates the phenomenon of interference which is the central notion behind correlation spectroscopy). By the Principle of Superposition, the electric field at any point in space is simply the sum of electric fields. Thus, at a point on the screen, the electric field is given by

$$\tilde{E}_S(x, t) = \tilde{E}_1(x, t) + \tilde{E}_2(x, t) = E_{01}e^{i(kx - \omega t + \phi_1)} + E_{02}e^{i(kx - \omega t + \phi_2)} \quad (1.22)$$

What is seen on the screen, however, is the intensity rather than the electric field. Using Eq. 1.3, we can write

$$I_S = \frac{\langle \tilde{E}_S \tilde{E}_S^* \rangle}{2\eta} \quad (1.23)$$

$$= \frac{\langle \tilde{E}_1 \tilde{E}_1^* \rangle + \langle \tilde{E}_2 \tilde{E}_2^* \rangle + \langle \tilde{E}_1 \tilde{E}_2^* \rangle + \langle \tilde{E}_1^* \tilde{E}_2 \rangle}{2\eta} \quad (1.24)$$

$$= \frac{E_{01}^2 + E_{02}^2 + 2E_{01}E_{02}\cos(\phi_1 - \phi_2)}{2\eta} \quad (1.25)$$

$$= I_1 + I_2 + I_{12} \quad (1.26)$$

where  $I_{12}$  is called the interference term. Clearly, it depends on the relative phase of the electric fields. If they are in phase, i.e.  $\phi_1 - \phi_2 = k2\pi$  (for any integer  $k$ ), then the intensity is greater than the sum of the two intensities. If they are  $180^\circ$  out of phase, i.e.  $\phi_1 - \phi_2 = k\pi$  ( $k \neq 0$ ), then the intensity is less than the sum.

## Coherence

Temporal self-coherence of light describes its longitudinal phase properties. In broad terms, the coherence time of an electromagnetic wave is the length of time for which its phase remains constant. Monochromatic light, for example has an infinite coherence time. Truly monochromatic light, however cannot exist. Eq. 1.2 implies that the electromagnetic field is an ideal harmonic (i.e. single sinusoid) wave and extends infinitely in time and the phase  $\phi$  stays the same for all time. Clearly this cannot be true since all waves have a finite temporal extent.

Light is generated as a result of electrons transitioning between energy states, which are typically on the order of several nanoseconds in duration. An idealized version of the wave

packet at a given point in space could be represented by

$$E_{packet}(t) = \begin{cases} E_0 \cos(\omega t), & -T \leq t \leq T \\ 0, & \text{otherwise} \end{cases} \quad (1.27)$$

One can then think of a light wave as a succession of such wave packets. The average duration of such a wave packet is the coherence time  $\delta t_c$  (a more rigorous definition will be given shortly). In practice, the coherence time is further limited and a wave cannot be described using a single sinusoid even for its finite duration. Fluctuations and collisions among the molecules of the light source cause Doppler shifts and discontinuities in the wave.

Temporal coherence is, of course, not a binary phenomenon. The phase at time  $t$  and  $t + \tau$  is likely to be highly correlated for small  $\tau$  and become less correlated as  $\tau$  increases. To quantify this, we use the self-coherence function, given by

$$\tilde{\Gamma}_{11}(\tau) = \left\langle \tilde{E}(t + \tau) \tilde{E}^*(t) \right\rangle \quad (1.28)$$

where  $\tilde{E}(t)$  is complex, and we omit the explicit dependence on  $x$  since the discussion is limited to a single position in space. This is the autocorrelation function of the electric field. This function, however, depends on the amplitude of  $\tilde{E}(t)$  so it is useful to consider the normalized form, called the complex degree of temporal coherence:

$$\tilde{\gamma}_{11}(\tau) = \frac{\tilde{\Gamma}_{11}(\tau)}{\tilde{\Gamma}_{11}(0)} = \frac{\left\langle \tilde{E}(t + \tau) \tilde{E}^*(t) \right\rangle}{\left\langle \tilde{E}(t) \tilde{E}^*(t) \right\rangle} \quad (1.29)$$

such that the peak value is 1. Note that this is a complex quantity, so for example a

monochromatic wave has a complex degree of coherence given by

$$\tilde{\gamma}_{11} = e^{-i\omega\tau} \quad (1.30)$$

The degree of coherence is given by the magnitude of this quantity, so a monochromatic wave has complete coherence,  $|\tilde{\gamma}_{11}| = 1$ . To summarize:

$$|\tilde{\gamma}_{11}| = 1, \text{ coherent limit} \quad (1.31)$$

$$0 < |\tilde{\gamma}_{11}| < 1, \text{ partial coherence} \quad (1.32)$$

$$|\tilde{\gamma}_{11}| = 0, \text{ incoherent limit} \quad (1.33)$$

For a more detailed introduction to the concept of the degree of coherence, see [33, ch. 12].

## Fourier transforms

Coherence can also be understood in terms of the spectral composition of a light source. The ideal monochromatic wave consists of a single frequency, and thus its spectrum is an infinitely narrow peak at that frequency.

The frequency spectrum of a wave is related to its temporal profile through the Fourier transform

$$S(\omega) = \int_{-\infty}^{\infty} \tilde{E}(t) e^{i\omega t} dt \quad (1.34)$$

and vice versa through the inverse Fourier transform

$$\tilde{E}(t) = \frac{1}{2\pi} \int_{-\infty}^{\infty} S(\omega) e^{-i\omega t} d\omega \quad (1.35)$$



where  $S(\omega)$  is the complex amplitude of the light at frequency  $\omega$ . Eq. 1.35 can be interpreted to mean that  $\tilde{E}(t)$  is simply a weighted summation of sinusoids  $e^{-i\omega t}$ , weighted by their spectral amplitude  $S(\omega)$ . Monochromatic light, for instance, contains a single frequency  $\omega_0$ , so  $S(\omega) = E_0\delta(\omega - \omega_0)$  and the integral in Eq. 1.35 simplifies to Eq. 1.2. To create more complex, waveforms, we must sum up a broader range of frequencies. For instance, the wavepacket given by Eq. 1.27 has a spectrum given by  $S(\omega) = E_0T\text{sinc}(T(\omega - \omega_0))$ . The coherence time  $\Delta t_c$  is therefore defined to be inversely proportional to the width of the spectrum

$$\Delta t_c = \frac{1}{\Delta\nu} = \frac{2\pi}{\Delta\omega} \quad (1.36)$$

We may also choose to refer to the coherence length, which is related to the coherence time by the speed of light

$$\Delta l_c = c\Delta t_c \quad (1.37)$$

White light, such as that from an incandescent bulb, consists of a large range of frequencies, which encompass the entire visible range. The spectrum is very broad, and therefore the coherence time is short. Laser light, in contrast, famous for its high coherence, has a very narrow spectrum and may be referred to as quasi-monochromatic. That is, for relatively long intervals the field it produces can be described with a single sinusoid. As such, when we refer to “coherent” light, we typically mean “quasi-monochromatic,” i.e. having a long coherence time.

### 1.2.2 Dynamic Light Scattering (DLS)

To lay the groundwork for a discussion of the “diffuse correlation spectroscopy” portion of TD-DCS, we begin with a description of a more fundamental technique from which DCS is derived. Dynamic light scattering (DLS), also referred to as quasi-elastic light scattering

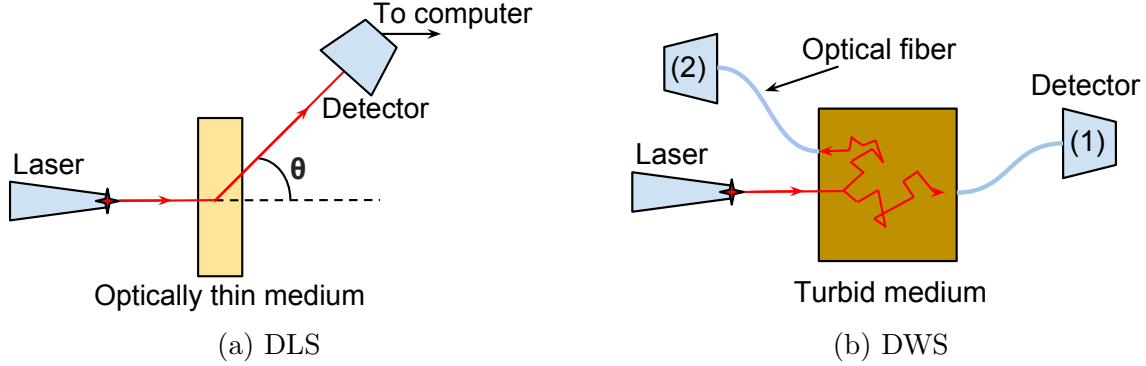


Figure 1.8: (a) Experiment schematic for DLS, with the detector positioned at angle  $\theta$ . (b) Experiment schematic for DWS. Note that the detector can be positioned in either the transmission (1) or reflectance (2) geometry, and there is no longer a well-defined scattering angle since the light is propagating diffusely through the medium.

(QELS) or photon correlation spectroscopy (PCS), has a wide range of applications, and there is a large body of theoretical and experimental work devoted to it [34, 35, 36, 37].

In its original form, DLS is used to estimate particle sizes in a solution by measuring its diffusivity, or diffusion constant  $D_B$ . For example, under some assumptions, we can use the Stokes-Einstein relationship  $D_B = \frac{k_B T}{6\pi\eta R}$  to calculate the particle's radius  $R$ . Depending on the application, this principle may also be referred to by other names: laser Doppler velocimetry (LDV), electrophoretic light scattering (ELS), Doppler shift spectroscopy (DSS), and others, depending on the exact measurement setup and application [34, ch. 1.4]. In biomedical applications, it may be referred to as laser speckle contrast imaging (LSCI) and can be used to estimate blood flow [15, ch. 5]. In this section, we discuss only the small portion of the DLS theory and applications that is critical for further discussion of DWS (§1.2.3) and DCS (§1.2.4).

The basic experimental setup for DLS is diagrammed in Fig. 1.8a. A coherent light wave impinges on a volume and is scattered in all directions. A detector is placed at angle  $\theta$  from the source light path and measures the scattered light. As a result of motion of the particles, the scattered light is Doppler shifted to a different frequency, depending on the direction and

speed of the particle's motion. Since there is now light of various frequencies impinging on the detector, this results in a broadening of the spectrum. By the discussion in the previous section, this corresponds to a decrease in the degree of coherence of the light.

The alternative interpretation of this phenomenon is directly from the intensity autocorrelation function. If the particles were motionless (c.f. static light scattering (SLS) [38]), the scattered field from one particle would differ in phase from the fields scattered from the other particles and thus create an interference pattern in the far-field known as a speckle pattern (Fig. 1.9). Now, suppose the particles are in motion. If we observe a single point in the pattern, e.g. a fixed location on a screen where the speckle pattern is projected, called a speckle, the intensity at that point would fluctuate due to changes in phase caused by particle motion. As described in §1.2.1, phase differences cause either destructive or constructive interference, so changes in phase cause variations in the interference pattern. If we record the intensity from the speckle as it changes over time, we can measure how well correlated the intensity at time  $t$  is to the intensity at time  $t + \tau$ . This is quantified using an autocorrelation function, as discussed in §1.2.1.

The time-varying speckle and laser Doppler approaches can be shown to be identical [39], since the autocorrelation function is related to the power spectrum through the Fourier transform, as stated by the Wiener-Khinchin theorem. Although we can measure the spectrum directly, modern instrumentation provides better resolution by making measurements in the time domain, so we restrict our discussion to the time-varying intensity of a speckle, characterized by the autocorrelation function.

Using the notation most common in the field,  $G_1(\tau) = \langle E(t)E^*(t + \tau) \rangle$  is the unnormalized field autocorrelation function, identical to  $\Gamma_{11}(\tau)$  from Eq. 1.28, where  $E(t)$  is the

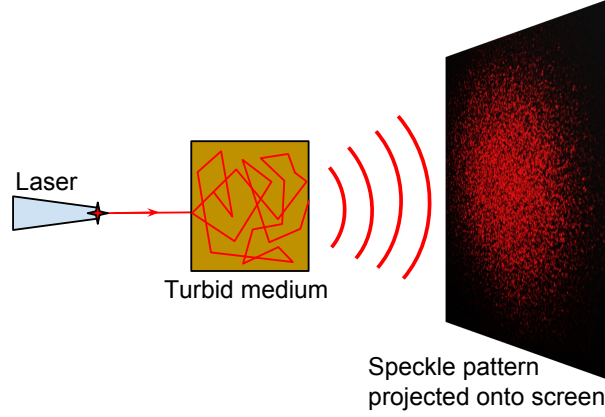


Figure 1.9: A speckle pattern created by coherent light being scattered through a turbid medium.

complex amplitude (the explicit phasor notation  $\tilde{E}(t)$  is omitted). Similarly,

$$g_1(\tau) = \frac{G_1(\tau)}{G_1(0)} = \frac{\langle E(t)E^*(t + \tau) \rangle}{\langle E(t)E^*(t) \rangle} \quad (1.38)$$

is the normalized version. Often,  $G_1$  and  $g_1$  are instead given as the magnitude of the field autocorrelation, i.e. as the degree of coherence (Eq. 1.31). What is measured by a detector, however, is the intensity, from which we can compute the unnormalized intensity autocorrelation function  $G_2(\tau) = \langle I(t)I(t + \tau) \rangle$ . We again can normalize this to avoid having to factor in the average intensity into our calculations, and the normalized intensity autocorrelation function is given by

$$g_2(\tau) = \frac{G_2(\tau)}{G_2(0)} = \frac{\langle I(t)I(t + \tau) \rangle}{\langle I(t) \rangle^2} \quad (1.39)$$

Under certain assumptions [37, ch. 2.3.3.1], the intensity autocorrelation  $g_2$  can then be

related to the field autocorrelation  $g_1$  by what is known as the *Siegert relation*<sup>1</sup>:

$$G_2(\tau) = G_1(0)^2 + |G_1(\tau)|^2 \quad (1.40)$$

$$\text{or } g_2(\tau) = 1 + |g_1(\tau)|^2 \quad (1.41)$$

According to Eq. 1.41, the maximum value for the normalized intensity autocorrelation is 2, and it decays to 1 with larger lags  $\tau$  (note that the range is not from 1 to 0 as one might expect due to the average intensity term  $G_1(0)^2$ ). The above equation, however, is only true for a single point in space. As might be seen from the example speckle pattern in Fig. 1.9, the intensity fluctuations at two points far apart on the screen are entirely independent from one another. So, if we average the intensity over the entire screen, the total intensity fluctuation will be almost zero, even though the fluctuation at any single point is strong. On the other hand, two points that are very close to each other might be expected to fluctuate at the same rate. This idea is quantified by the *coherence area*  $A_{coh}$ , i.e. the area on the screen in which the fluctuations will be the same [35, ch. 2.3.3]. If  $A$  is the total detected area, then  $N_{coh} = \frac{A}{A_{coh}}$  is the number of coherence areas seen by the detector. So, for a DLS experiment, the maximum value for the normalized intensity autocorrelation is inversely proportional to the number of coherence areas detected. In modern literature, the Siegert relation is usually stated as

$$g_2(\tau) = 1 + \beta |g_1(\tau)|^2 \quad (1.42)$$

where the  $\beta$  term ranges from 0 to 1 and corrects for the spatial and temporal coherence of the light in the experimental setup. To maximize  $\beta$ , we would like to measure from a single coherence area (i.e. one speckle in the speckle pattern).

The simplest way to measure the intensity autocorrelation is by a direct recording of

---

<sup>1</sup>This relation was originally obtained in the context of radar signal processing [40]

the scattered light, where the output current of the detector is linearly proportional to the intensity of the light impinging on it. The plot of intensity over time can then be used to calculate the intensity autocorrelation according to Eq. 1.39. In the case of low light intensity, we can use an alternative method known as photon counting. As the name implies, the detector (either a photomultiplier tube or an avalanche photodiode must be used for sensitivity) outputs a pulse when a single photon is detected. This stream of impulses can then be also directly autocorrelated with Eq. 1.39. Importantly, it can be shown from photon counting statistics that the photon correlation is equal to the intensity correlation [37, ch. 2.3.2.3]. The origin of the term “photon correlation spectroscopy” is now clear – we are using the self-correlation of the scattered photon stream to make inferences about the scattering medium.

As a simple example, we present the autocorrelation for a solution of non-interacting colloidal monodisperse spherical particles undergoing Brownian diffusion, as derived in [37, ch. 16.2.2] or [41] (analogous derivations in [36], [34]). Scattered field is given by the superposition of the scattered fields from each of the  $N$  particles with which the light interacted (note we are now describing the field in all three dimensions):

$$E_S(t) = \sum_{j=1}^N E_0 e^{i(\omega_0 t - \mathbf{q} \cdot \mathbf{r}_j(t))} \quad (1.43)$$

where  $\mathbf{q} = \mathbf{k}_s - \mathbf{k}_{in}$  is defined as the scattering wavevector and  $\mathbf{r}_j(t)$  is the time-varying position of the  $j^{\text{th}}$  particle. Substituting Eq. 1.43 into Eq. 1.38 and using the assumptions given above about the medium, the normalized field autocorrelation function can be calculated to be

$$g_1(\tau) = e^{-q^2 D_B \tau} = e^{-(2k_0 \sin \frac{\theta}{2})^2 D_B \tau} \quad (1.44)$$

where  $q = |\mathbf{q}| = 2k_0 \sin \frac{\theta}{2}$  is the magnitude of the scattering wavevector, and  $k_0 = \frac{2\pi}{\lambda}$  is the

wavenumber of the light in the medium. That is, given a light of a certain wavelength and scattering angle impinging on a medium with a Brownian diffusion coefficient  $D_B$ , the correlation between the intensity at time  $t$  and the intensity at time  $t + \tau$  decreases exponentially with increasing  $\tau$ . The critical assumption in the calculations is that the light is scattered exactly once, which can be satisfied in practice, for example, if the solution is sufficiently dilute. The case of multiple scattering events is discussed in §1.2.3.

Finally, having a theoretical form for  $g_2(\tau)$  using the Siegert relationship, as well as the measured intensity autocorrelation function, we can attempt to estimate the parameters of interest, in this case  $D_B$ , by fitting the theoretical form of  $g_2$  to the measured function. While in theory it is possible to calculate  $\beta$  from first principles [37, ch. 2.3.3.2], it is more practical to instead incorporate it into the fitting algorithm as well. We iteratively try to find the optimal value for  $\beta$  and  $D_B$  until the optimal goodness-of-fit is reached. See [37, ch. 4.1,4.4] for a description of many of the fitting algorithms used in this context.

### 1.2.3 Diffusing Wave Spectroscopy (DWS)

Like DLS, diffusing wave spectroscopy was originally studied in the context of particle motion and sizing but has since been extended to biomedical applications [42]. First proposed by Maret and Wolf in 1986 [43], diffusing wave spectroscopy (DWS) complements DLS by removing the assumption that light is scattered from the medium exactly once. In contrast, DWS assumes the strong multiple-scattering limit of light and, like NIRS, propagation through tissue can be modeled as a diffusion process. Following the same simple example from the previous section of non-interacting monodisperse spherical diffusing particles, instead of assuming light is scattered once we instead assume that the sample is thick or concentrated enough that the light passing through it has scattered many times. Let's first assume we know the length of the path a photon traveled,  $s$ . The field autocorrelation

function can then be calculated to be

$$g_1(s, \tau) = e^{-2k_0^2 D_B \tau \frac{s}{l^*}} \quad (1.45)$$

where  $l^* = \frac{1}{\mu'_s}$  is the transport mean free path (i.e. the expected distance a photon travels before begin scattered, corrected for anisotropy, analogous to the definition of  $\mu_s$  in §1.1.1).

Comparing to Eq. 1.44, observe that the  $q^2 = (2k_0 \sin \frac{\theta}{2})^2$  term has now been replaced simply by  $2k_0^2$ . Intuitively, since we no longer have a defined scattering angle, we replace  $\sin \frac{\theta}{2}$  with its average value,  $\langle \sin \frac{\theta}{2} \rangle = \frac{1}{2}$ . Further observe the additional term  $\frac{s}{l^*}$ , corresponding to the number of random walk steps the photon took over its path of length  $s$ . This term implies that every scattering step, on average, causes a decay of  $e^{2k_0^2 D \tau}$  in the autocorrelation. In other words, in comparison to the single-scattering decay in Eq. 1.44, the multiple scattering light decorrelates by a factor of  $\frac{s}{l^*}$  more quickly.

Without more involved instrumentation (c.f. [44]), we cannot measure the pathlength traveled by a photon, so we need to consider all possible pathlengths. The total field autocorrelation function is then a weighted average over all possible pathlengths, given by

$$g_1(\tau) = \int_0^\infty P(s) g_1(s, \tau) ds \quad (1.46)$$

where  $P(s)$  is the probability that a photon traveled distance  $s$ . A rigorous derivation can be found in [37, ch. 16.2.3.1] or [45].

To calculate the closed-form theoretical autocorrelation function, it remains to determine the pathlength distribution function  $P(s)$ . In fact, this question has already been addressed in §1.1.4 when discussing the theoretical form of the temporal point spread function (TPSF).  $P(s)$  is exactly the TPSF of the tissue, normalized such that it is a valid probability distribution, and where the pathlength can be simply related to time-of-flight as  $s = t \cdot v$ , where  $v$  is



the speed of light in the medium. Thus  $P(s)$  can be modeled using Monte Carlo simulations, or solving the radiative transport equation with the appropriate conditions e.g. Eq. 1.21.

In general,  $P(s)$  and therefore  $g_1$  will depend on the optical properties of the medium, the physical dimensions of the medium, and the measurement geometry. For example, in the case of a semi-infinite homogeneous diffusing medium in a reflectance geometry, using Eq. 1.21 to obtain  $P(s)$  and Eq. 1.45 for  $g_1(s, \tau)$ ,  $g_1(\tau)$  can be calculated to be

$$g_1(\tau) = \frac{\exp\left(-\frac{z_0}{l^*} \sqrt{6k_0^2 D_B \tau}\right)}{1 + \frac{2}{3} \sqrt{6k_0^2 D_B \tau}} \quad (1.47)$$

where for the purpose of modeling, the source of the diffusing light intensity is a distance of  $z_0$  inside the boundary of the medium. This approximates placing the light source at the surface and assuming it becomes diffusive after progressing a distance of  $z_0$  into the medium. Typically,  $z_0 = l^* = \frac{1}{\mu'_s}$ . For an in-depth discussion, see [45, Section 4] or [37, ch. 16.2.3.4].

It may be preferable to measure  $P(s)$  directly. Using the same principles that time-domain NIRS uses to estimate the differential path factor (DPF), we can find  $P(s)$  by directly measuring the photon time-of-flight. We can limit our measurements to photons of known pathlength by time-gating techniques (§1.1.4) and use the pathlength-dependent autocorrelation function  $g_1(s, \tau)$  to estimate the dynamical properties. This technique is known as pulsed diffusing-wave spectroscopy [44].

The experimental setup for DWS is shown in Fig. 1.8b. As with DLS, we collect the light intensity over time from a single speckle, and measure the autocorrelation function. In the DWS case, however, there is no well-defined scattering angle as a result of multiple scattering. This allows us to make the measurements in either the reflectance or transmission geometry. For the analysis, given an appropriate theoretical model for  $g_2$  we can find the model parameters which result in the best match with the measured autocorrelation.

One important consequence of the multiple scattering, is that light loses all of its polar-

ization properties as it scatters through the medium. Assuming the source light is linearly polarized, the detected light polarization will have equal amplitudes both parallel and perpendicular to the initial polarization direction. Since the two polarizations of light are independent from one another, this has the same effect as measuring light from two speckles – their intensity fluctuations will average out. As a result, without the use of a polarization analyzer at the detector, the maximum value for  $\beta$  is 0.5, rather than 1 as seen before. An analyzer would restore the maximum value of  $\beta$  to 1 at the expense of half of the light intensity. See [37, ch. 16.3.1] for an in-depth discussion.

Furthermore, due to the multiple scattering, the photon pathlength through the medium is much longer than for a DLS experiment, and therefore it is critical that the coherence length of the laser is longer than the pathlength. Otherwise, the autocorrelation function will decrease as a result of short coherence length rather than from the effects of scattering. This phenomenon is addressed in greater detail in §2.3.3.

### 1.2.4 Diffuse Correlation Spectroscopy (CW-DCS)

Although this technique is currently referred to in the literature simply as “DCS,” when necessary to differentiate it from the time-domain variant that is the focus of this thesis, we refer to it as continuous-wave diffuse correlation spectroscopy (CW-DCS), alluding to the fact that (just like DLS and DWS) it uses a continuous-wave laser source. Indeed, “diffuse correlation spectroscopy” is simply a renaming of DWS, appropriating the term for use in a blood flow monitoring context, analogous to “laser speckle contrast imaging” [15, ch. 5] referring to DLS for blood flow monitoring. The term “DCS,” originating in the Yodh lab [46], has become the one used in this field as it is more descriptive of the underlying signal acquisition process which relies on the correlation of diffusing photons.

The modern iteration of CW-DCS uses a theoretical formalism different from the one

introduced in the previous section, although the solutions are largely the same. The assumptions made by the DWS theory are too restrictive and in some cases, particularly the backscattering (reflection) geometry, do not fully explain experimental data. Specifically, the theory predicts slower decay rate at large delay times than that seen experimentally [37, ch. 16.2.4] and thus requires ad-hoc correction terms [37, ch. 16.2.3.4]. In 1992, Ackerson et al. [47] proposed an alternative formulation suggesting an abstraction where correlation itself is being “transported” through the medium. Mathematically, they propose that the correlation gets transported through the medium in the same way that light does, and suggest a formalism analogous to the radiative transport (RT) equation (Eq. 1.8) called the correlation transport (CT) equation.

$$\begin{aligned} \frac{1}{c} \frac{\partial G_1(r, \Omega, \tau, t)}{\partial t} \Omega \cdot \nabla G_1(r, \Omega, t, \tau) + \mu_t G_1(r, \Omega, \tau, t) \\ = \mu_s \int G_1(r, \Omega, \tau, t) g_1^s(\Omega, \Omega', \tau) f(\Omega, \Omega') d\Omega' + S(r, \Omega) \end{aligned} \quad (1.48)$$

The advantage of this formulation is that not only does it reduce to the single-scattering theory from DLS and the multiple-scattering theory from DWS with the appropriate conditions, but also allows for more general applicability, using the same mathematical tools that are used for analyzing radiative transport [47, 48].

One such mathematical tool, discussed earlier in the context of the RTE, is the diffusion approximation in a highly scattering medium (Eq. 1.9). In 1995, Boas et al. [49] proposed modeling the correlation transport in turbid media as a correlation diffusion, stating the equation for a homogeneous colloid (as in the example used in the previous sections):

$$\left( -\frac{1}{3\mu'_s} \nabla^2 + \mu_a + 2\mu'_s k_0^2 \alpha D_B \tau \right) G_1(r, \tau) = S(r) \quad (1.49)$$

Comparing this with the photon diffusion equation (Eq. 1.9), we see that in addition to the

photon absorption term  $\mu_a$  we have a “correlation absorption” term  $2\mu'_s k_0^2 \alpha D_B \tau$  which accounts for the drop in correlation during the “correlation diffusion.” See [41] for a derivation.

Although, as with the photon diffusion equation, solving this for arbitrary configurations is difficult, certain solutions exist. For example, in a homogeneous semi-infinite medium, the unnormalized field autocorrelation function  $G_1$  is given by [6]

$$G_1(\tau) = \frac{vS_0}{4\pi D} \left[ \frac{e^{-K(\tau)r_1}}{r_1} - \frac{e^{-K(\tau)r_2}}{r_2} \right] \quad (1.50)$$

where the variables are defined as in Eq. 1.12–1.16, and

$$K(\tau) = \sqrt{3\mu_a\mu'_s + \mu'_s k_0^2 6\alpha D_B \tau} \quad (1.51)$$

Unsurprisingly, this has a functional form is identical to the steady-state photon flux given by Eq. 1.10, since they are both solutions to their respective diffusion equations. The parameter  $\alpha D_B$  is referred to as the blood flow index (BFi) and is a measure of perfusion through the tissue.  $D_B$  is, as before, the Brownian diffusion coefficient<sup>1</sup> and  $\alpha$  is the tissue blood volume fraction – a term to account for scattering from only the moving particles in the tissue [46]. We can then compute  $g_1$  following Eq. 1.28 as  $g_1(\tau) = \frac{G_1(\tau)}{G_1(0)}$  and  $g_2$  using the Siegert relation (Eq. 1.42).

The experimental setup is similar to DWS (Fig. 1.8b), although optical fibers typically deliver light from the source to the medium as well as from the medium to the detector. (For an introductory discussion on fiber optics, see [33, ch. 5.6]). To couple the light from the source to the medium, a multimode fiber is typically used, with core diameters ranging from 50 to 200  $\mu\text{m}$  to maximize power transmitted to the medium. Various numerical aperture values can be used. Generally, higher values are easier to couple to the laser, and lower

---

<sup>1</sup>It may seem counterintuitive to use a diffusion model to estimate blood flow, but in practice we see that this model fits the data very well [6] and may have reasonable justification [46].

values minimize divergence of the beam at the output therefore decreasing the possibility of contaminating the measurement with reflected light [28, ch. 6.2].

As with DLS, we would like to measure the light from a single speckle, however in the multiple-scattering setting a speckle is typically on the order of  $1\mu\text{m}$  in diameter. It is therefore more practical to use a single-mode fiber which, by propagating a single spatial mode, acts as a spatial filter, resulting in perfect spatial coherence in the cross-section of the fiber [50]. In practice, since we're using unpolarized light, there are actually two orthogonal modes corresponding to both polarization directions. Therefore, as discussed in §1.2.3,  $\beta$  can be no larger than 0.5. For further discussion on single- and multi-mode fibers in DLS and DWS, see [51, 50].

We conclude this section with a discussion of the limitations of CW-DCS. As evident from Eq. 1.50, fitting the autocorrelation function requires prior knowledge of the absorption and scattering coefficients of the tissue. Often, as is done in the CW-NIRS case (§1.1.2), the optical properties are taken as the average over the probed volume and across subjects. These values can be found in a table such as [14, ch. 5] or [15, ch. 1]. Due to the high variability between subjects and anatomical locations, this results in a high error in flow estimates [52]. Alternatively, the optical properties can be found by performing NIRS and CW-DCS measurements concurrently [46, 7], which requires separate hardware and software and thus more bulky and expensive instrumentation. Finally, similar to CW- and FD-NIRS, the photons travel through layers of tissue that confound the measurement. In our primary application of neuromonitoring, unwanted signal comes from the scalp, skull, and subdural layers Fig. 1.6. Since we are only interested in cerebral blood flow, this is clearly undesirable. These issues are addressed by a novel technique that combines the time-domain principles of TD-NIRS for estimating optical properties and making time-gated measurements with the CW-DCS methodology of estimating dynamical properties.

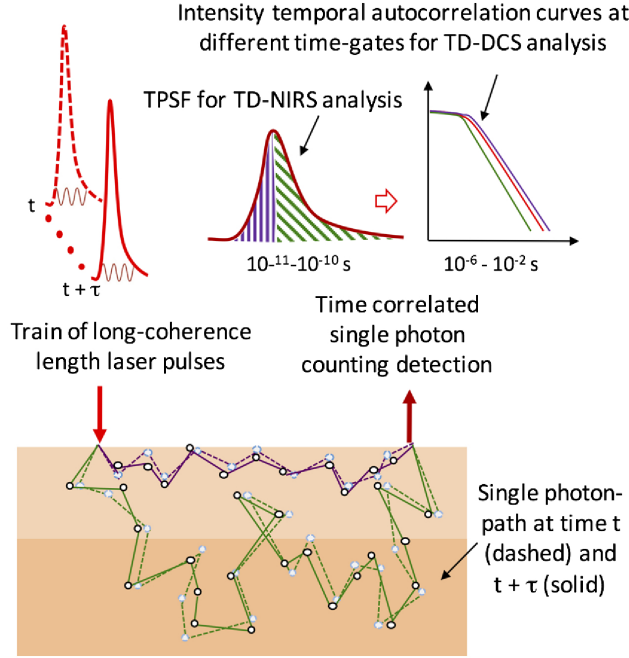


Figure 1.10: Illustration of the main concept behind time-domain diffuse correlation spectroscopy. Reprinted from [54].

### 1.2.5 Time-Domain Diffuse Correlation Spectroscopy (TD-DCS)

In 2015 it was proposed [53], instead of using continuous-wave light as in CW-DCS, to use laser pulses, analogous to TD-NIRS or pulsed DWS, and simultaneously measure both the TPSF and the autocorrelation. See Fig. 1.10 for an illustration of this idea. The first advantage is clear: using a time-domain measurement, exactly like TD-NIRS, we can measure the TPSF of the tissue and therefore use the photon diffusion theories developed for TD-NIRS to estimate the tissue optical properties directly. Thus, we eliminate a large portion of the error in estimating dynamical properties that is caused by imprecise optical property values [54].

Taking advantage of time-correlated single photon counting strategies described in §1.1.4 and §1.2.2, we can furthermore effectively combine the instrumentation necessary for TD-NIRS and CW-DCS. Recall that the TCSPC implementation of TD-NIRS records the time-

of-flight (TOF) of each through the tissue, and histograms all of the collected photons based on their TOF to produce the TPSF. Similarly, the photon counting implementation of DLS records the absolute arrival time (i.e. the time from the start of the experiment) for each photon, and using that information computes the measured intensity autocorrelation. Using the terminology of [32], for TD-DCS we record *both* the photon time-of-flight (referred to as the *micro* time) and the absolute arrival time (referred to as the *macro* time). Histogramming the time-of-flight allows us to compute the TPSF and estimate optical properties, and the arrival time allows us to compute the autocorrelation and estimate the dynamical properties.

The third major advantage of TD-DCS is gained from time-gating techniques that are in principle the same as those for time-gated TD-NIRS or pulsed DWS, although are implemented in a much more straightforward fashion. Like the other time-domain techniques, TD-DCS allows us to constrain our measurement to a subset of photons with known pathlength. It is assumed that photons with a longer pathlength traveled deeper into the medium before reaching the detector, while those with a shorter pathlength took a more direct path from the source to the detector, reaching only superficial layers. (Fig. 1.10) Effectively, through time-of-flight measurements, we acquire depth resolution (TOF is linearly related to pathlength by the speed of light in the medium). Thus, if we only compute the autocorrelation using photons with time-of-flight less than a certain threshold, we estimate the dynamical properties of the superficial layers, and conversely deeper layers using long TOFs.

There is one aspect, however, in which the time-domain requirements directly conflict with those for DCS. On the one hand, in TD-NIRS, the laser pulses are as short as possible, possibly as low as 3-4 picoseconds wide. As discussed in §1.1.4, this is to minimize the convolution effect of the source/detector system response with the “true” TPSF of the medium. To resolve the TPSF, the temporal pulse width must be less than the time from the start

of the TPSF to the peak. On the other hand, DCS relies on the long temporal coherence length of the laser, and is assumed to be infinite in the theoretical derivations. Even in the ideal case, the temporal coherence of a pulse of light cannot be longer than the width of the pulse itself. In practice, phase artifacts such as “chirp” in the electric field further decrease the coherence length. Intuitively, a pulse cannot be in phase with itself beyond the point where it has decayed, since there is no phase to speak of. The degree of coherence (§1.2.1) has dropped effectively to zero for lags greater than the pulse width.

Formally, the spectrum (found mathematically by means of the Fourier transform) of a perfectly coherent (i.e. monochromatic/single-frequency/harmonic and therefore extending infinitely in time) wave is a  $\delta$ -function (i.e. an infinitely narrow impulse). In contrast, a pulse can be thought of as the product of a harmonic wave with a finite-length envelope. In the Fourier domain, this is the convolution of a  $\delta$ -function with the Fourier transform of the envelope, so the spectrum is broadened and the coherence length, which is inversely proportional to the spectrum width, is shorter (§1.2.1).

Pulses in the range of 100-500ps satisfy both requirements. First, the TPSF width is typically on the order of several nanoseconds so pulses in that range are sufficiently narrow. Furthermore, it was demonstrated according to the theory developed by Bellini et. al. [55], a transform-limited 300ps pulse in a medium with typical biological optical properties, although would suffer a reduction in the signal-to-noise ratio (SNR), would have a long enough coherence length to make a reasonably robust measurement [53]. The effects of finite temporal coherence are discussed in greater depth in §2.3.3.



# Chapter 2

## Completed Work

Having set the theoretical ground for time-domain diffuse correlation spectroscopy and alluded to some of the instrumentation, as well as experimental and computational techniques involved in estimating optical and dynamical properties of turbid media, we now discuss in detail the prototype construction, the initial measurements, and theoretical modeling that was done over the course of this project. These are clearly only the first steps and there is much more development to be done and theory to be explored.

### 2.1 Instrument prototype construction

The primary challenge in meeting the conflicting narrow-pulse-width and long-coherence requirements of TD-DCS is in constructing the laser source and detector hardware. A practical requirement for making measurements is to have a high photon flux, so a custom source laser with high peak power must be designed, and sensitive time-correlated single photon counting detectors must be used.

The final system design is shown in Fig. 2.4. For this thesis work, only a subset of the system was implemented to demonstrate proof-of-concept, which we refer to as “first

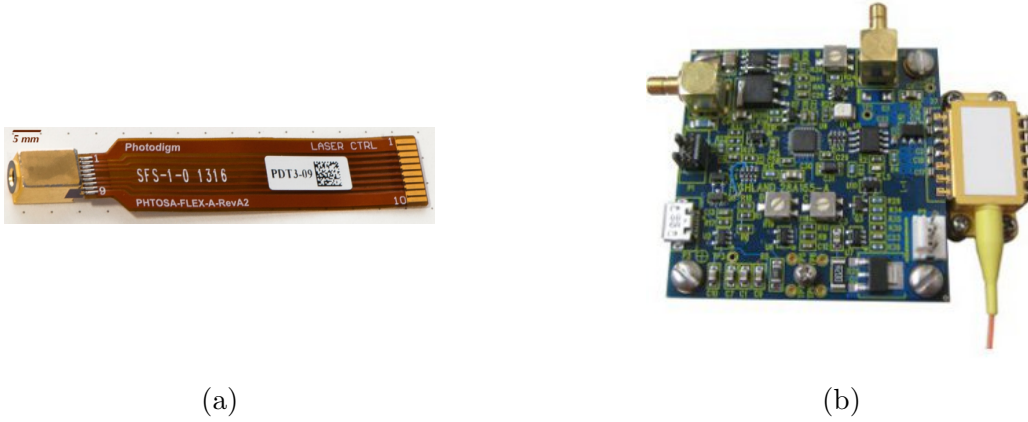


Figure 2.1: (a) Photodigm Mercury TOSA package (b) Highland T165 pulse board with connected Type-1 butterfly-packaged laser.

generation,” and used for initial measurements. The “second generation” system was used in subsequent data collection for the theoretical discussion in §2.3.3.

### First generation

The source laser is a distributed Bragg reflector (DBR) laser (PH852DBR280TS, Photodigm, Inc.), with nominal light wavelength of 852 nanometers, continuous-wave coherence of 10 meters and 180 milliwatt average optical power (480 mW peak power). The pulses are created by electrically gain-switching the seed laser using a commercial picosecond pulsed laser driver (T165-9, Highland Technology, Inc.). Although the maximum repetition rate at which the TPSFs (4-5 ns long) from consecutive pulses will not overlap is 200MHz, the pulse board repetition rate is variable and we used it at no more than 150MHz. The pulse board also specifies that it is possible to vary the pulse width by injecting current pulses of varying width into the laser, but we found that the pulse width could not be increased beyond 100ps without corrupting the pulse shape, likely due to the physical limitations of the laser.

The primary challenge here is controlling the laser with the pulse board. The laser comes in a Mercury TOSA package (Fig. 2.1a) where due to the length of the ribbon cable, there

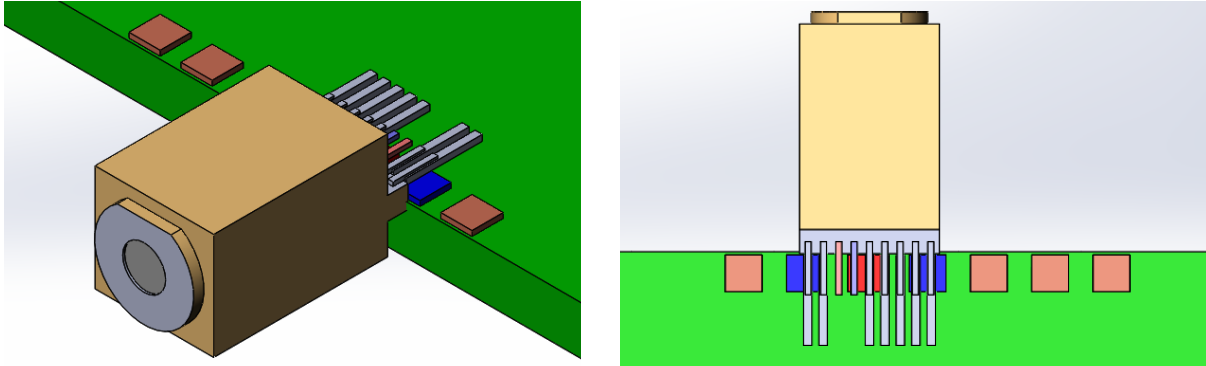


Figure 2.2: SolidWorks model of the laser and pulse board connection. Copper pads represent electronic connections to the pulse board. For both the board and the laser, the cathode is shown in red and the anode in blue. Original files can be found at <https://github.com/dtyulman/tddcs>

is an excess parasitic inductance. While this is not an issue in the CW operation for which it was designed, for our pulsed operation the cable must be removed and the laser pins connected directly to the pulse board. Furthermore, the pulse board connector is designed with a pin socket connection for a Type-1 butterfly-packaged laser diode (Fig. 2.1b) that is incompatible with our laser. As such, the pin sockets must be removed and the laser pins soldered directly to the copper pads to which the pin sockets were attached. To account for the mismatch in pin spacing as shown in Fig. 2.2, the gap is simply filled with solder – an inelegant but effective solution.

The second challenge in the construction of the custom system is effectively coupling the light into the medium. The laser is mounted onto a custom machined aluminum frame as shown in Fig. 2.3. The frame serves both as a heatsink and as an adapter for off-the-shelf hardware used to for further shaping the laser beam. First, to avoid backreflections that may damage the laser, it is necessary to install an optical isolator at the output of the laser. For the 852nm wavelength of our laser, we used Thorlabs model IO-3D-850-VLP. To accurately position the isolator into the beam’s path we mounted the isolator onto a Cage XY Translator (Thorlabs CXY-1) which was centered on the custom laser frame using 6mm

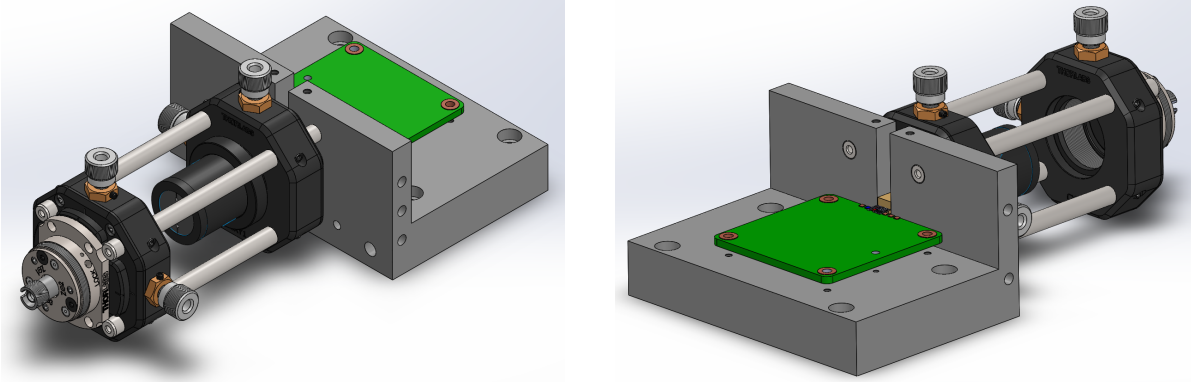


Figure 2.3: SolidWorks model of the custom pulsed laser assembly. In the final construction, the assembly is bolted to a monolithic heatsink (not shown). Original files can be found at <https://github.com/dtyulman/tddcs>

diameter aluminum rods (Thorlabs ER4) as shown. Finally, to couple the light into an optical fiber for delivery into the medium, we used an adjustable FiberPort (Thorlabs PAF-X-15-PC-B). To mount the FiberPort onto our cage setup we used another XY translator which we modified with four screw holes to attach the FiberPort directly to the translating component. The FiberPort then offers an FC connection to an optical fiber. For our experiments, as with DCS, light is delivered to the medium using a multimode fiber.

On the detection side, as with the other photon correlation techniques, to maximize  $\beta$  and therefore the SNR, we would like to limit the detection area to a single speckle. In practice, this is not achievable so, as with DCS [28, Section 6.2], we instead use a single-mode fiber to collect scattered light from the medium and deliver it to the detector. For our experiments, 5.6 micrometer single-mode silica fibers are used. The detector is a novel red-enhanced, single-photon avalanche diode detector (SPAD), with a high temporal resolution, from the SPADlab at the Politecnico de Milano [56, 57].

Although a custom time-to-digital converter (TDC) card is included in the final design, for the first-generation prototype we use an off-the-shelf Becker & Hickl GmbH SPC-600 [32] card to record the micro and macro photon arrival times. Although it was originally

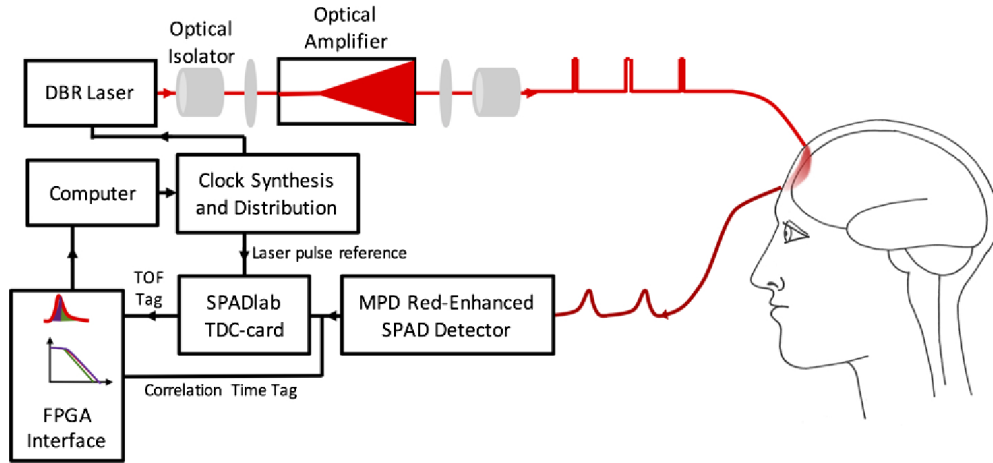


Figure 2.4: Schematic of the TD-DCS instrumentation. Reprinted from [54].

designed for fluorescence correlation spectroscopy [31, 32], the data collection technique is identical<sup>1</sup>. The photon arrival data was then exported from the Becker & Hickl software for offline data analysis (§2.2).

## Second generation

Since the construction of the original prototype, the second-stage amplification was added to the laser source using a pumped taper diode amplifier (m2k-TA-0850-3000-DHP, m2k-laser GmbH), allowing much higher peak power to be used in experiments [58, 59]. Furthermore, the development of the custom data acquisition hardware was completed, incorporating the time-to-digital converter (TDC) card with the custom FPGA firmware to measure photon timing, and a USB3 interface (Cypress EZ-USB FX3) to transfer photon data to the computer. Furthermore, an alternative pulsed laser source was acquired (PicoQuant CPDL-S-760) with a nominal wavelength of 760nm, used in the experiments for §2.3.3.

<sup>1</sup>The signal for FCS, of course, is different – the source of light is fluorescent markers on molecules

## 2.2 Data analysis methods

### 2.2.1 Computing the temporal point spread function

As discussed in the previous section, we use time-correlated single photon counting methods to record the *micro* and *macro* times of the photons. To compute the TPSF, we can use the exact approach discussed in §1.1.4 and simply histogram the micro times (i.e. time-of-flight) for many photons to estimate the distribution of intensity over time. There are, however, several instrumentation-specific considerations to be addressed.

#### Reversed start-stop

Many TCSPC modules, including the Becker & Hickl SPC-600 and our custom time-to-digital converter, operate in what is known as “reversed start-stop” mode. In this setup, rather than recording the time starting at the generation of the input laser pulse and stopping at the arrival of a photon, the “stopwatch” starts running at the arrival time of a photon, and stops at the generation of the next laser pulse. The advantage of this method is that since photons are typically detected at a much lower rate than the input pulse train (i.e. there is less than one photon detected on average from each laser pulse), we only need to operate the hardware at the photon detection rate, rather than the much higher laser pulse rate [32]. This is easy to compensate for by simply reversing the time axis of the histogrammed TPSF.

#### Folding

When recording signals with very high repetition rates it may be necessary to record the TPSF over several periods of the pulsed laser. That is, instead of using every laser pulse as the time-of-flight reference, we might use every other one, or every fourth, and so on. The Becker & Hickl SPC-600 card allows frequency division values of  $d = 1, 2, 4, 8$ , or  $16$ .

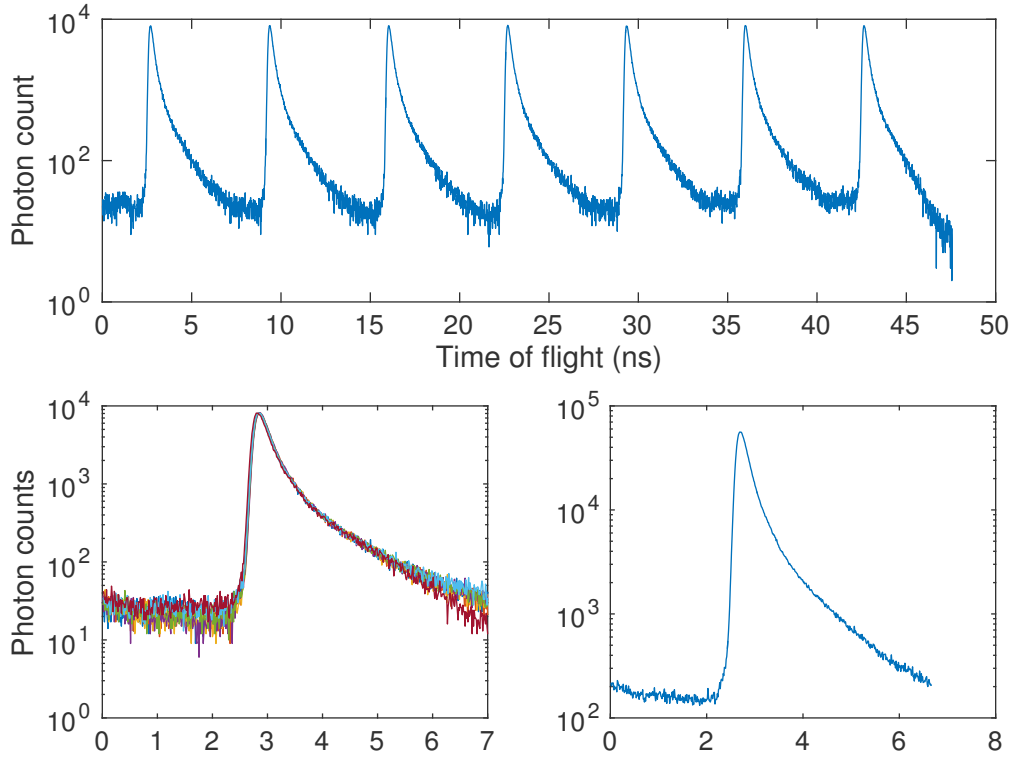


Figure 2.5: TPSF folding. Top plot shows an example of a time-of-flight histogram collected using a Becker & Hickl SPC-600 card with the frequency divider set to 8 (the eighth peak is out of range and therefore not recorded). Bottom left shows all the individual peaks shifted to line up with the first (each peak shown in its own color). Bottom right shows the sum of all the peaks to create the final TPSF (note the decrease in noise and the y-scale).

Of course, we can only work with a single TPSF. One option is to pick one period of the recorded histogram and delete all of the other photons. This is clearly unfavorable since we are only using  $1/d$  of the recorded photons for analysis and thus unnecessarily reducing the signal-to-noise ratio. A much better approach is to fold all of the histograms onto one, as shown in Fig. 2.5

We would like to simply shift the  $k^{\text{th}}$  additional “sub-TPSF” to the left by  $kT$  where  $T$  is the time between two consecutive pulses. In reality, however, the micro time is discretized: in Fig. 2.5, for instance, we have 4096 discrete time bins spanning 50ns. Since the repetition rate of the laser  $T$  (e.g.  $\frac{1}{100\text{MHz}}$ ) is typically not an integer multiple of the time resolution of

the micro time (e.g.  $\frac{50\text{ns}}{4096}$ ), a more careful folding procedure is necessary. We compute the autocorrelation function of the raw histogrammed signal. The peaks in the autocorrelation function then will correspond to the lags of the raw signal for which it is most similar with itself. Since all of the TPSFs in the raw signal should be identical, the lag values for the autocorrelation peaks are the precise values by which we should shift each “sub-TPSF” for the best overlap with the first “sub-TPSF.” We can then subtract the shifts from the raw stored micro times accordingly. The implementation to perform the folding directly on the TPSF is provided in §A.6 and on the raw micro times in §A.7.

### 2.2.2 Estimating $\mu_a$ and $\mu'_s$

One of the advantages of TD-DCS is the capability of estimating the tissue optical parameters concurrently with the measurements of the dynamical properties. Having computed the temporal point spread function as in the previous section, we can then analyze it using all of the computational tools developed for TD-NIRS [29]. Although this aspect is outside of the scope of this thesis, we include a brief discussion for completeness.

As mentioned in §1.1.4, the measured TPSF is actually not the true impulse response of the system. It is a convolution of the pathlength distribution function of the medium (i.e. the “true” impulse response of the medium) with the impulse response function (IRF) of the laser source and detection system. The resulting measured TPSF is therefore a broadened version of the true TPSF. In TD-NIRS, the laser pulses are a few picoseconds wide, and compared to the width of the “true” TPSF are negligible, so it is valid to ignore the broadening effects due to the instrumentation. Thus, we can directly fit the measured TPSF to estimate  $\mu_a$  and  $\mu'_s$ . However, due to the coherence length requirements of DCS, we must use wider pulses that are hundreds of picoseconds and are no longer negligible compared to the width of the “true” TPSF, so fitting the measured TPSF directly will result in an error that is an



increasing function of the pulse width.

To compensate for this broadening, there are several deconvolution algorithms that attempt to remove the broadening effects of the instrumentation IRF. Deconvolution, however, is in general an ill-posed inverse problem that does not have a unique solution. Solving ill-posed problems can be considered an entire field in itself, and we do not discuss it further. See [14, ch. 20] for discussion of this issue in the context of TD-NIRS. An alternative approach may be to pre-convolve the theoretical TPSF with the measured IRF before fitting. In this approach, rather than attempting to remove the effects of the IRF from the measured TPSF, we are fitting to the data a function that already has the IRF factored into it.

### 2.2.3 Computing the autocorrelation function

As discussed in §1.2, to estimate the dynamic properties of the medium, we measure the time-averaged autocorrelation function of the scattered light intensity  $g_2(\tau) = \frac{\langle I(0)I(\tau) \rangle}{\langle I(0) \rangle^2}$  and find the parameters of the appropriate model to best fit the measured data. In this section we discuss the algorithms to compute this function from the photon-counting data. Since the intensity autocorrelation is equal to the photon autocorrelation, we will use  $I(t)$  to denote the photon stream.

#### Direct summation

In general, by definition, the autocorrelation function  $R(\cdot)$  of an arbitrary discrete-time signal  $f(\cdot)$  is given by the convolution

$$R(\tau) = (f * \bar{f})(\tau) \equiv \sum_{t \in \mathbb{Z}} f(t) \bar{f}(t - \tau) = \sum_{t \in \mathbb{Z}} f(t) f(t + \tau) \quad (2.1)$$

where  $\bar{f}(t) = f(-t)$ .

Using this definition, given the intensity of the photon stream as a function of time, we can directly evaluate this sum for every value of  $\tau$ . This procedure, however, is time-consuming since only the photon arrival times are recorded and therefore must be converted to a temporal-raster form. For a measurement  $L$  seconds long at a sampling frequency  $\omega_s$ , this is a vector of length  $T = L\omega_s$ , containing a 1 if a photon arrived within that time bin and 0 otherwise, (e.g. if the vector of photon “macro” times is  $\mathbf{m} = (1, 4, 5, 7)$ , then  $I(t) = (1, 0, 0, 1, 1, 0, 1)$ , see §A.1).

Since  $I$  is a finite-length vector (or alternatively, we can consider it to be a discrete-time function that is equal to zero outside of the interval  $[0, T]$ ), it only makes sense to compute  $R(\tau)$  for  $\tau \leq T$ , since  $R(\tau) = 0$  for  $\tau > T$ . Furthermore, we are not interested in lags beyond which the signal has fully decorrelated, so we only need to consider  $\tau \leq \tau_{max}$ . In our application,  $\tau_{max} \ll T$ . Thus, the computational complexity of this algorithm is  $\Theta(T \cdot \tau_{max})$  since we are summing  $T$  terms  $\tau_{max}$  times.

Finally, note that computing the autocorrelation of the intensity  $I(t)$  according to Eq. 2.1 results in the *unnormalized* autocorrelation  $G_2(\tau)$ . Normalizing, we get

$$g_2(\tau) = \frac{T}{N^2} G_2(\tau) \quad (2.2)$$

where  $N$  is the total number of photons collected and  $T$  is the number of time bins as defined above, so  $G_2(0) = \frac{N^2}{T}$

### Fast Fourier transform

Since the convolution of two signals in the time-domain is equivalent to their multiplication in the Fourier domain [60], given an arbitrary function  $f(t)$  we can instead compute  $F(k)$ ,

its discrete Fourier transform (DFT) (note that this is the discrete analog of Eq. 1.34)

$$F(k) = \mathcal{F}\{f\} \equiv \sum_{t=0}^{T-1} f(t) e^{-\frac{2\pi j k t}{T}}, \quad k \in \mathbb{Z} \quad (2.3)$$

and compute the autocorrelation by

$$R(\tau) = \mathcal{F}^{-1} \{ \mathcal{F}\{f\} \cdot \mathcal{F}\{\bar{f}\} \} \quad (2.4)$$

where the inverse DFT is given by

$$\mathcal{F}^{-1}\{F\} \equiv \sum_{k=0}^{T-1} F(k) e^{+\frac{2\pi j k t}{T}}, \quad k \in \mathbb{Z} \quad (2.5)$$

The fast Fourier transform (FFT) algorithm allows us to compute the DFT as well as the inverse DFT with computational complexity  $\Theta(T \log T)$ . The element-wise multiplication in the Fourier domain takes  $\Theta(T)$  time, so the entire algorithm has computational complexity  $\Theta(T \log T)$  [61, ch. 30]. Note that this method does not allow us to specify the longest lag we are interested in  $\tau_{max}$  and computes the autocorrelation for all of the values of  $\tau$  such that  $f(t)$  and  $f(t + \tau)$  overlap. In other words,  $\tau_{max} = T$ . As before, letting  $f(t) = I(t)$  in Eq. 2.4 gives us  $G_2(\tau)$  so to compute  $g_2(\tau)$  normalization is done as in the previous section.

### Histogrammed interarrival times

A much faster method for our application operates directly on the photon arrival times. To see the equivalence of this method with the direct summation method described above, consider Eq. 2.1. First, observe that in our application,  $f(t) = 0$  or  $1 \forall t$ , so if  $R(\tau) = k$  for some  $\tau$ , then there were exactly  $k$  pairs of photons arriving  $\tau$  time steps apart. Therefore, for every value of  $\tau$  we are interested in, we would like to count all pairs of photons that are

$\tau$  time steps apart. The algorithm is outlined as follows.

Suppose we have recorded a length- $N$  vector  $\mathbf{m}$  of photon arrival times (i.e. “macro” times). We initialize a length- $\tau_{max}$  array of zeros  $R$  that we will use to histogram the interarrival times of the photon pairs.

The  $i^{th}$  iteration of the algorithm considers entry  $m_i$  in  $\mathbf{m}$  as the first photon of a pair. It then, one by one, looks at all the subsequent photons  $m_j$ , ( $j > i$ ) and calculates  $m_j - m_i$ , the interarrival time of the photon pair. Suppose  $m_j - m_i = \tau$ , so we increment  $R(\tau) \leftarrow R(\tau) + 1$ . Once we reach an entry  $m_{j^*}$  such that  $m_{j^*} - m_i > \tau_{max}$ , we stop this iteration since  $\mathbf{m}$  is a strictly increasing sequence and we know  $m_k - m_i > \tau_{max}$  for all  $k > j^*$ . We increment  $i$  and begin the next iteration. We iterate until  $i = N$  and all the photon pairs that are less than  $\tau_{max}$  seconds apart have been considered.

If we were interested in computing the longest possible lag (i.e.  $\tau_{max} = T$ ), we would have to consider all pairs of photons, so the worst-case computational complexity is  $O(N^2)$ . Note that this is a function of the number of photons  $N$ , rather than the time of the experiment  $T$ . Since we are only interested in lags  $\tau \leq \tau_{max}$ , the complexity is actually much better since each iteration only looks at photons that arrived less than  $\tau_{max}$  seconds after the one under consideration for that iteration. If the average flux is  $\phi$  photons per time step, the expected number of pairs of photons considered in each iteration is  $\phi\tau_{max}$  (note  $\phi T = N$ ). Therefore, in expectation the runtime is  $\Theta(N \cdot \phi\tau_{max})$ .

What we have computed in the vector  $R$  is, in fact, the unnormalized measured intensity autocorrelation function  $G_2(\tau)$ . Once again, we normalize these values as before to compute  $g_2(\tau)$ . See §A.2 for an implementation of this algorithm.

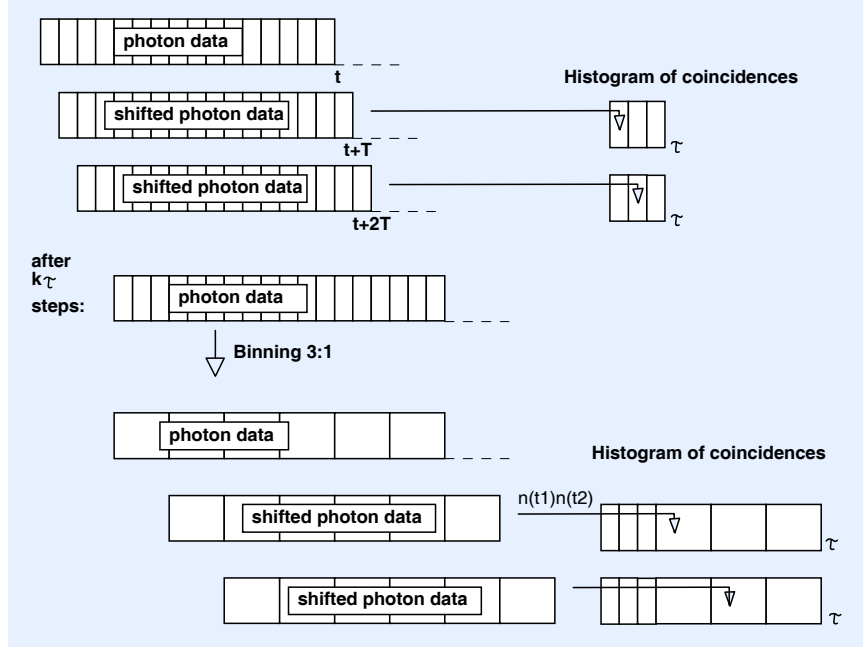


Figure 2.6: Autocorrelation with progressive binning. Reprinted from [32, p. 461]

### Progressive binning/Multiple tau

For completeness, we include an alternative fast method for computing the autocorrelation function, as used in the Becker & Hickl photon counting software, [32] as it is representative of the ideas used in many of the current digital correlators.

We begin by computing the autocorrelation as in 2.1. In other words, after converting the photon arrival times to the temporal-raster form, we shift our signal to get  $I(t + \tau)$ , element-wise multiply  $I(t)$  and  $I(t + \tau)$ , and sum all the values in the resulting vector. After  $k_\tau$  shifts (where  $k_\tau$  is a user-defined parameter), we re-bin the photon-arrival raster by a factor of three: for every three time bins of length  $l$  we replace it with a single time bin of length  $3l$ , and if a photon arrived in any of the three original time bins, the new bin contains a 1 and 0 otherwise. We then compute the autocorrelation on the re-binned signal as described. We continue this process (Fig. 2.6) until we reach the desired number of lags.

Note that due to the repeated re-binning of the photon stream, this procedure only

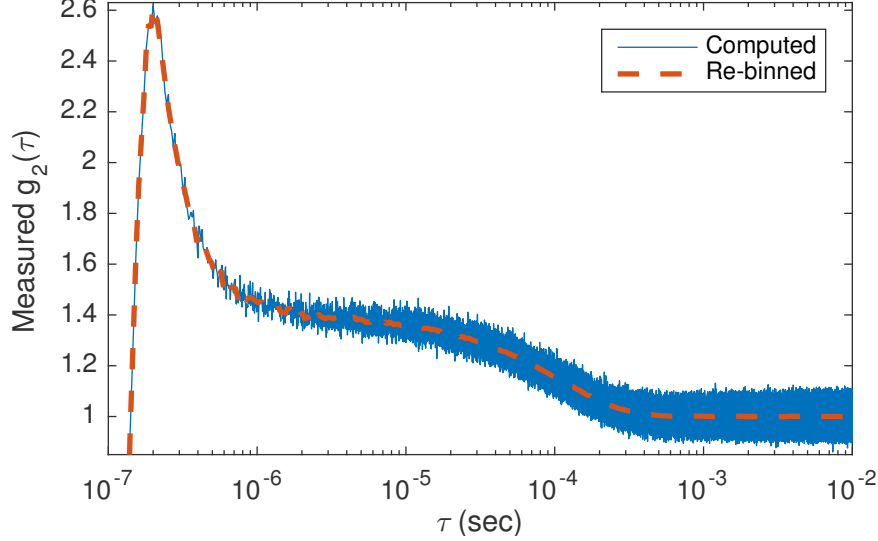


Figure 2.7: Exact autocorrelation computed by histogramming interarrival times and re-binned with progressively larger bins ( $k_\tau = 30$ ) for visualization. (Note that the peak at the smallest lags is an artifact due to the detection hardware. Since unpolarized light was used here, the maximum value for  $\beta$  is 0.5)

calculates an estimate of the autocorrelation function, thus there is a trade-off between runtime and accuracy [62].

To reduce noise, although we perform the autocorrelation using the histogramming method described above, for display purposes we re-bin the results to look like the results produced by a multi-tau algorithm (Fig. 2.7). Observe that with longer lag times, there are fewer photons contributing to the autocorrelation so the noise increases. Thus, it makes sense to smooth the autocorrelation function by an increasingly wider window. See §A.3 for an implementation.

## 2.2.4 Estimating $\beta$ and BFi

Having computed the measured autocorrelation function as in the previous section, we can attempt to estimate the model parameters of interest. Although we can estimate  $\mu_a$  and  $\mu'_s$  by fitting the theoretical TPSF to the measured data as is done in practice for TD-NIRS

(§1.1.4 or §2.2.2), for reliability in these experiments, we measure the optical properties of the medium independently using a commercial FD-NIRS instrument [63].

Since in our experimental setup the source-detector separation is sufficiently small compared to the depth and surface area of the phantom, we estimate it as a semi-infinite medium. The theoretical DCS autocorrelation function for a semi-infinite medium in a reflectance setup is given by Eq. 1.50. We use the Levenberg-Marquardt algorithm [64], a common nonlinear least squares fitting procedure, to find the blood flow index (BFi, given by  $\alpha D$  in Eq. 1.50) parameter which results in the closest match between the data and the theoretical form.

Since what we have measured, however, is the intensity autocorrelation function  $g_2$ , related to  $g_1$  through Eq. 1.42, there is another unknown parameter  $\beta$  that needs to be estimated. Since  $\beta$  depends on the spatial and temporal coherence properties of the light in the experimental setup, it is practical to directly fit this value simultaneously with the BFi.

It is also important to note, however, that due to artifacts such as afterpulsing which arise from feedback in the detector hardware [65], the autocorrelation values for the smallest values of  $\tau$  is not valid and should be ignored for the purposes of fitting. As shown in Fig. 2.8, only a subset of the measured autocorrelation curve is used for the fitting procedure. The range for fitting is chosen visually, although the typical minimum lag used is around  $10^{-5}$  seconds. The implementation for estimating the parameters is given in §A.4, using the  $g_2(\tau)$  function defined in §A.5.

### 2.2.5 Time-gating the photons

We now reach the essential aspect of time-domain diffuse correlation spectroscopy – time-gating the photons and thus measuring the autocorrelation using a subset of photons that traveled a fixed pathlength through the medium. Since measurements are performed in the

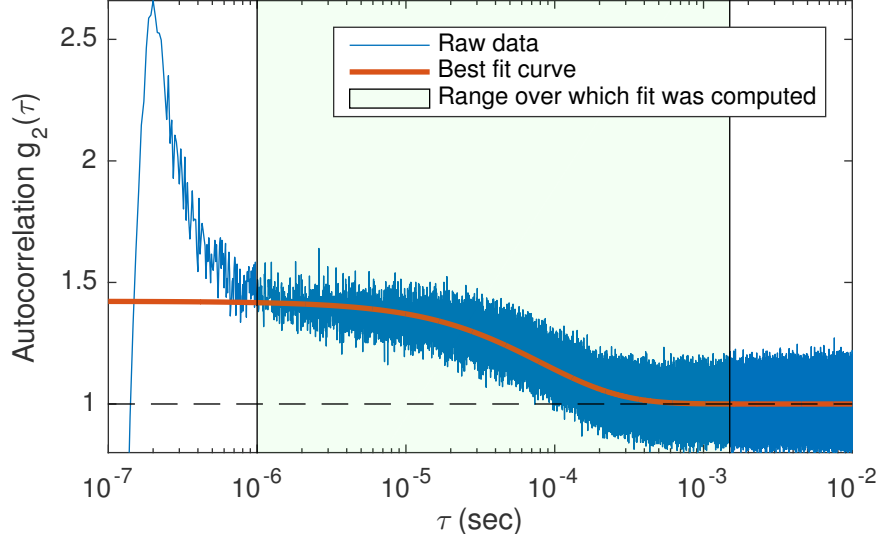


Figure 2.8: The computed autocorrelation function and the best model that fits the data. Short lags are invalid and are ignored for the purpose of fitting the data.

reflectance geometry (Fig. 1.3b), short pathlengths correspond to photons in the superficial layers, and long pathlengths to photons in the deeper layers. Thus, in the neuromonitoring setting, if we compute the autocorrelation of “deep” photons, we can measure the cortical blood flow avoiding the confounds from the superficial layers.

Since we have the recording of the full photon stream with micro and macro times for each photon, we can simply select the photons whose micro times correspond to the portion of the TPSF we wish to analyze. Having selected the photons with micro times within a specified range, we then compute the autocorrelation using only that subset of photons. We then fit that autocorrelation using the appropriate model as described in the previous section to estimate the BFi in the corresponding layer of the medium.



## 2.3 Results

In this section, we discuss the three primary experiments conducted for validation of various aspects of the TD-DCS technique. All of the measurements are conducted using “phantoms” – artificial objects designed to mimic biological samples for the purposes of device testing. Milk is a common choice for phantoms for diffuse near-infrared biomedical optical devices, due to its high scattering and low absorption coefficients resembling biological tissue, as well as its low price and easy availability. Liquid silicone as well as a polystyrene microsphere solution were also used for other phantoms, described in detail in the following subsections.

### 2.3.1 Initial measurements

For the initial test of TD-DCS using the first-generation system, we measured the flow properties for four different dilutions of whole milk with water (1:0, 1:1, 1:2, and 1:3 milk-to-water ratios), as well as for a solution of polystyrene microspheres (1.73 $\mu\text{m}$  diameter, 0.0013 $\mu\text{m}^{-1}$  concentration, 1.55 refractive index). Due to the fat content in milk, its flow properties are temperature dependent and to normalize for this each of the five solutions was brought to room temperature (24°C). Due to the low average power of the pulsed laser without the amplifier to optimize the measured light intensity the measurement was made in a standard 12.5  $\times$  12.5  $\times$  45 mm cuvette in the transmission geometry. At  $\lambda = 850\text{nm}$ , the scattering coefficient for whole milk was assumed to be  $\mu'_s = 26\text{cm}^{-1}$ , and proportional to the concentration (i.e.  $\mu'_s = 13\text{cm}^{-1}$  for a 1:1 dilution,  $\mu'_s = 8.67\text{cm}^{-1}$  for 1:2,  $\mu'_s = 6.5\text{cm}^{-1}$  for 1:3). The scattering coefficient for the microspheres is calculated using Mie theory [66] to be  $\mu'_s = 4.9\text{cm}^{-1}$ . The absorption coefficient in all five samples was assumed to be equal to water,  $\mu'_a = 0.042\text{cm}^{-1}$ .

Each measurement was taken three times, both with the first-generation TD-DCS system and with a CW-DCS system for comparison. The results are summarized in Fig. 2.9. The

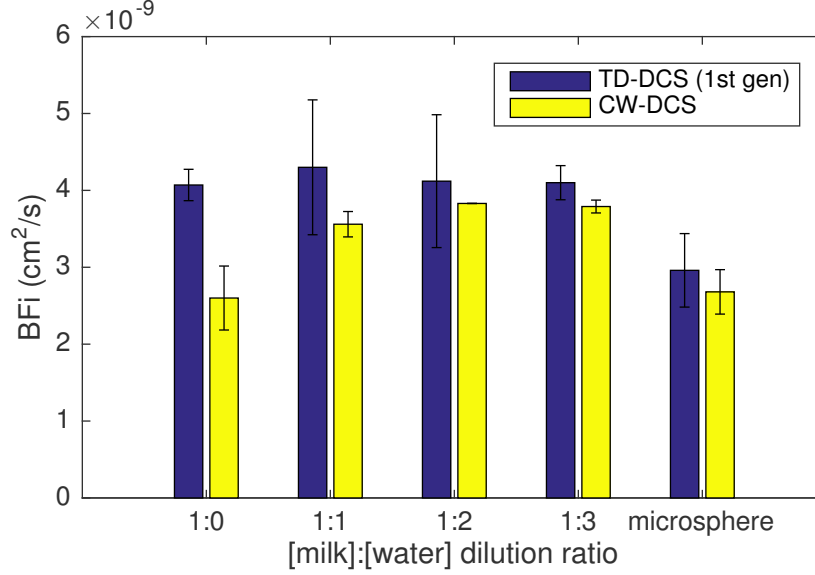


Figure 2.9: Initial BFi measurements using the first-generation TD-DCS system, in comparison with a state-of-the-art CW-DCS system. The average value over three separate measurements is shown, with error bars representing the standard deviation.

average values are reported, the error bars represent one standard deviation. As evident in the figure, the time-domain measurements systematically overestimate BFi (in this case it is equivalent to the Brownian diffusion coefficient  $D_B$ ). This is, in fact, contradictory to the results previously seen in the context of varying the coherence length of the source. Bellini et. al., for example, show a slower decay rate for measurements using short-coherence light in comparison to a coherent source [55].

### 2.3.2 Two-layer phantom

To validate the depth-resolving capabilities of TD-DCS, we perform measurements in a simple two-layer phantom. The phantom consists of two immiscible liquids with varying viscosities held in a standard 500mL beaker. The bottom layer is a 1-to-3 dilution of whole milk and water as in the previous section, and the top layer is liquid silicone with added pigment to modify its scattering properties. As above, the absorption and scattering coefficients for

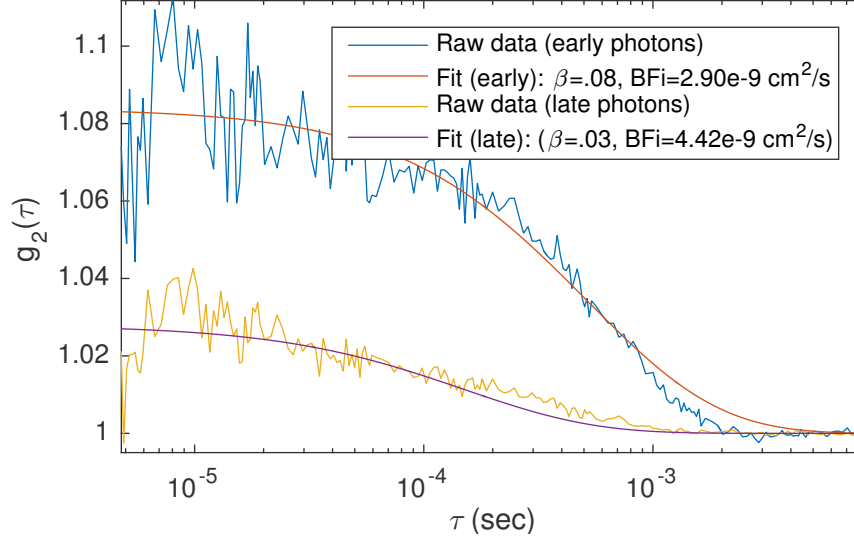


Figure 2.10: Autocorrelation curves and the corresponding BFi estimates computed in a two-layer phantom using only the early photons or only the late photons. As expected, the BFi is smaller for early photons, corresponding to the more viscous top layer.

diluted milk are  $\mu'_s = 6.5\text{cm}^{-1}$  and  $\mu'_a = .042\text{cm}^{-1}$ . For the liquid silicone  $\mu'_s = 3.7\text{cm}^{-1}$  and  $\mu'_a = .035\text{cm}^{-1}$ , measured using an FD-NIRS system [63].

Since the liquid silicone is qualitatively more viscous than diluted milk, we should expect that the BFi is lower in the top layer than the bottom layer. For the purposes of this analysis, all photons arriving prior to the peak of the TPSF are considered “early” and those arriving after the peak considered “late.” We compute two autocorrelation functions, using “early” and “late” photons and fit them with a semi-infinite homogeneous model to get a first estimate on the BFi values. The results are shown in Fig. 2.10 for a phantom with a 2.5mm thick layer of liquid silicon on the surface of the diluted milk. Although a semi-infinite model is not fully appropriate for this medium, as evidenced by the imperfect fit in the figure, we nevertheless see a 45% increase in BFi from the more viscous top layer to the bottom layer.

### 2.3.3 Measured vs. theoretical values of $\beta$

In all of the theoretical derivations and models of autocorrelation functions thus far, we have implicitly assumed that the coherence time of the laser source is infinite. In the case of CW-DCS, this is typically valid, since the coherence time of a continuous wave laser can be on the order of 30 nanoseconds (which, in a vacuum, equates to a coherence length of 9 meters). In comparison to the time-of-flight of a photon through tissue, which is no more than several nanoseconds, this is a valid assumption.

Not all laser sources, however, are that strongly coherent. In 1991 Bellini et. al. published a paper addressing the problem of making DLS and DWS measurements using a source with finite coherence length [55]. According to their model, assuming the spectrum of the laser source is Gaussian, the intensity autocorrelation function is given by

$$g_2(\tau) = 1 + \int_0^\infty \int_0^\infty P(s) P(s') g_1(s, \tau) g_1(s', \tau) e^{-2\left(\frac{s-s'}{l_c}\right)^2} ds ds' \quad (2.6)$$

Consider the photons traveling through the medium with a pathlength  $s$  and the photons with pathlength  $s'$ . If the difference in pathlengths  $s - s'$  is greater than the coherence length  $l_c$  of the light, the phase of the photons is uncorrelated simply by virtue of the coherence of the light itself, irrespective of the loss of coherence caused by scattering from moving particles in the medium. As a result, the baseline measured intensity autocorrelation function at lags greater than the coherence time will be considerably smaller than it would for a coherent light source. Since the time resolution of a typical correlator is not high enough to detect this baseline drop in autocorrelation, it appears that  $\beta$ , i.e. the value of  $g_2(\tau)$  with  $\tau$  extrapolated to zero, is significantly lower than it would be for coherent light. Thus, the *effective*  $\beta$  depends not only on the detected coherence area as discussed in §1.2.2, but also on the temporal coherence of the source.

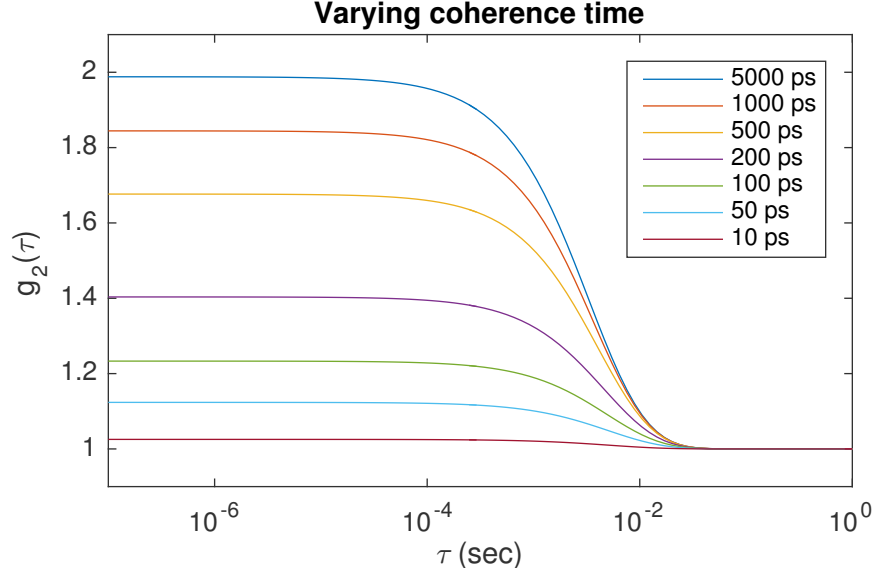


Figure 2.11: Simulated  $g_2(\tau)$  using Eq. 2.6, varying source coherence, for a homogeneous semi-infinite medium with  $g_1(s, \tau)$  given by Eq. 1.45 and  $P(s)$  given by normalizing Eq. 1.21,  $\mu_a = .05\text{cm}^{-1}$ ,  $\mu'_s = 1\text{cm}^{-1}$ ,  $\lambda = 800\text{nm}$ ,  $\rho = 10\text{mm}$ ,  $D_B = 10^{-9} \text{ cm}^2/\text{s}$

As noted before (§1.2.5), since we're using pulsed laser light, the temporal coherence length becomes upper bounded by the temporal width of the pulse. Thus, we can use Eq. 2.6 to model the intensity autocorrelation  $g_2$  for varying coherence lengths, as shown in Fig. 2.11. The code to run this simulation is provided in §A.8 Assuming the pulse is transform-limited, we simply set  $l_c = v\Delta t$ , where  $\Delta t$  is the temporal width of the pulse and  $v$  is the speed of light in the medium. Effectively, this models  $g_2$  using all of the photons from the TPSF. We would also like to investigate from a theoretical standpoint the effects of time-gating the photons as in §2.2.5.

To model the time-gating, we simply replace  $P(s)$  in Eq. 2.6 by  $P'(s)$ , a pathlength distribution that corresponds to the subset of pathlengths that are included in the time-gate, given by:

$$P'(s) = \frac{P(s) \text{rect}(s; s_{\min}, s_{\max})}{\int_0^\infty P(s) \text{rect}(s; s_{\min}, s_{\max}) ds} \quad (2.7)$$

where

$$\text{rect}(s; s_{\min}, s_{\max}) = \begin{cases} 1, & s_{\min} \leq s \leq s_{\max} \\ 0, & \text{otherwise} \end{cases} \quad (2.8)$$

is the rectangle, or boxcar, function that controls the limits of the time-gate by specifying the shortest and longest pathlengths to include in the gate,  $s_{\min}$  and  $s_{\max}$ , respectively. The denominator is an normalization term to ensure that  $P'(s)$  is a proper probability density function and integrates to 1.

### Varying gate width

The time-gating procedure removes all photons outside the specified gate limits, so only photons whose pathlengths differ by no more than  $s_{\max} - s_{\min}$  remain. Thus, we are computing the autocorrelation using photons which have similar pathlengths and thus have not lost their phase relationship simply by virtue of the finite coherence length. In the limiting case, if we consider only the photons which have a single pathlength  $s = s_{\min} = s_{\max}$ , the only contribution to their loss of coherence comes from interaction with the moving particles in the medium, and not from the coherence properties of the incident light<sup>1</sup>. Since coherence is not a binary phenomenon (§1.2.1), we would expect that wider time-gates would result in a lower value of  $\beta$ , with a maximum value of 0.5 (since we're using unpolarized light, c.f. §1.2.3) for an infinitely narrow gate as described above, and a minimum value equal to the CW value for an infinitely wide gate that considers all of the photons.

To demonstrate this behavior, we record data from a simple semi-infinite phantom and analyze the data with varying widths of the time-gate. The measurements are made with the second-generation system with the secondary PicoQuant laser ( $\lambda = 760\text{nm}$ ), as described in §2.1, using a 1-to-4 diluted whole milk phantom held in a standard 500mL beaker. A

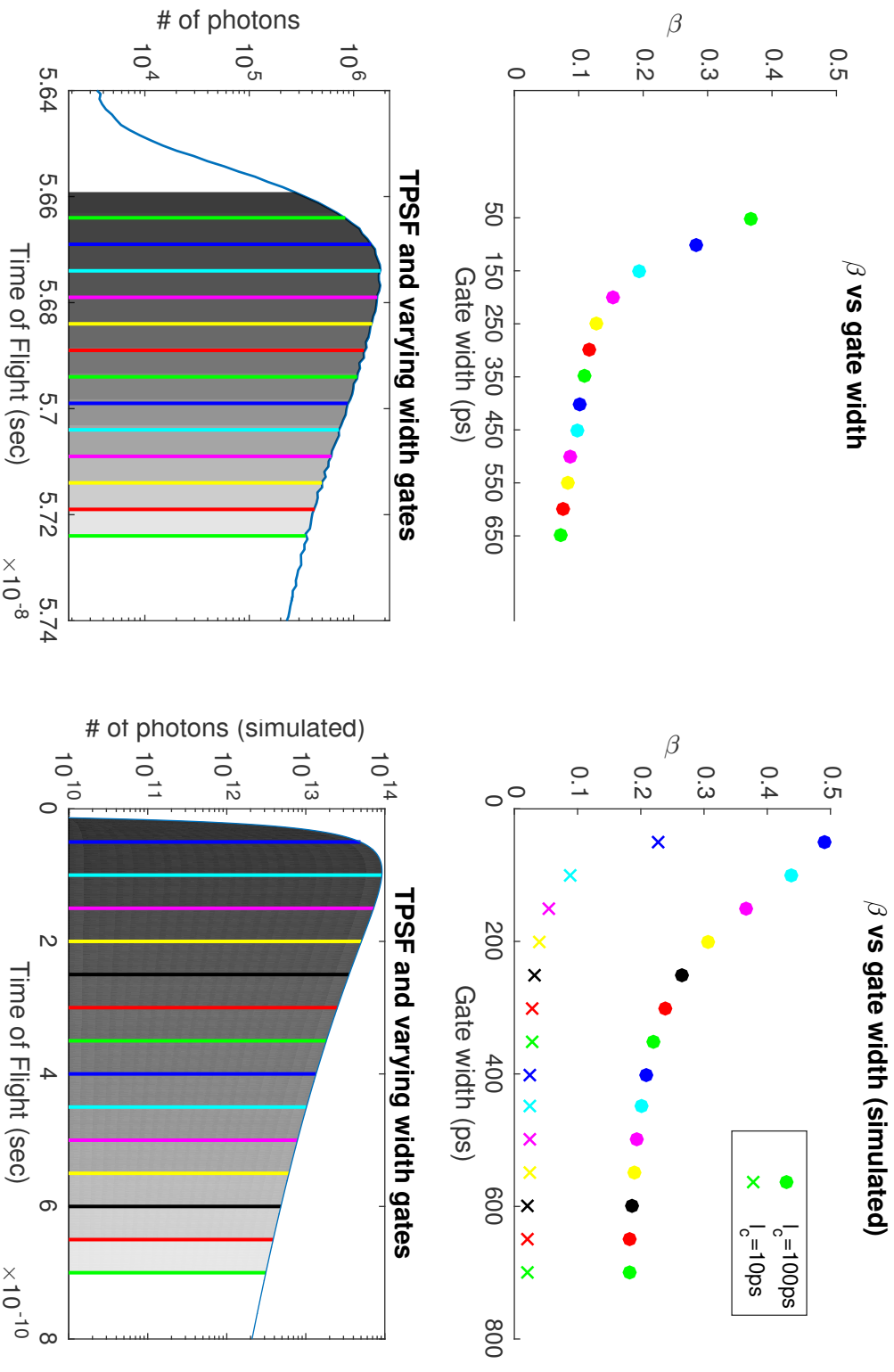
---

<sup>1</sup>This is why the coherence requirements for DLS are not as strict as for DWS or DCS: since the light is scattered exactly once, there is only one pathlength to consider.

reflectance geometry was used with the source and detector fibers lowered directly onto the surface of the liquid at three source-detector separations (5, 10, 15mm). These distances are small compared to the surface area and depth of the medium, which is therefore modeled as semi-infinite. We then compute the autocorrelation using subsets of photons corresponding to gate widths increasing in 50ps increments and find the value of the effective  $\beta$  for each one, following the analysis in §2.2.4. For the purpose of fitting in this experiment, the values of  $\mu_a = 0.51\text{cm}^{-1}$  and  $\mu'_s = 5.67\text{cm}^{-1}$  are obtained using a separate FD-NIRS system [63]. The results for a 10mm separation are shown in Fig. 2.12a.

To compare the results of the measurement with the theoretical predictions, we vary the gate width in the simulated model of  $g_2$  as described above, using theoretical models of  $g_1$  and  $P(s)$  for a semi-infinite homogeneous medium using the values of  $\mu_a$ ,  $\mu'_s$ ,  $\rho$ , and  $\lambda$  prescribed by the experimental setup. Note that since we are only looking at the value of  $\beta$ , i.e.  $g_2(\tau = 0)$ , the  $D_B$  parameter is irrelevant since it only affects the decay rate of the function and not the intercept. We assume that the pulses (100ps full width at half-max) are transform-limited and therefore the coherence length  $l_c = v \cdot [100\text{ps}]$  where  $v = \frac{c}{n}$  for the assumed refractive index of the medium  $n = 1.33$ . As the computed  $\beta$  values show in comparison with the measured values, this is likely to be an over-estimate. For perspective, we also calculate the values using an assumed coherence time of 10ps. The results for a 10mm separation are shown in Fig. 2.12b.

Although the simulations overestimate the absolute values of  $\beta$ , the simulated results shown a similar relative trend as the gate width increases, and a similar total drop in  $\beta$  from the shortest to the longest gate.



(a)

(b)

Figure 2.12: Effects of varying gate *width* on  $\beta$ , derived from (a) measurements and (b) simulations. All gates start at the leftmost edge and continue rightwards until the respective colored edge. Values of  $\beta$  are shown in corresponding colors.  $\rho = 10\text{mm}$ ,  $\mu_a = 0.51\text{cm}^{-1}$ ,  $\mu'_s = 5.67\text{cm}^{-1}$ .



### Varying gate delay

As has already been discussed, varying the delay of the time gate would give us the autocorrelation of subsets of photons which traveled different depths into the medium<sup>1</sup>, which enables the estimation of dynamical properties at varying depths. In practice, we also observe that increasing the gate delay results in a decrease in  $\beta$ .

To demonstrate this, we analyze the data from the semi-infinite homogeneous diluted milk phantom described above with a fixed 50ps gate width, and changing the gate delay in 50ps increments. An analogous simulation is performed for comparison. Results for the 10mm separation are shown in Fig. 2.13.

The limitations of this model are now more evident as fails to fully describe the observations. Notice that in the measured data,  $\beta$  continues to decrease with increasing gate delay, whereas according to the simulation it plateaus beyond the initial drop. Also note the relative drop in  $\beta$  for the simulation is extremely small, compared to the much more significant drop observed in the measurements. Furthermore, this cannot simply be explained by the coherence time of the laser, as evidenced by the points corresponding to the 10ps coherence time in the simulation, which exhibit a small initial drop and plateau.

## 2.4 Conclusions and further work

There are several further considerations to be addressed as immediate next steps after this work. When computing the depth-resolved flow values in §2.3.2, we arbitrarily split the TPSF into “early” and “late” photons using the peak as the midpoint. An alternative might be to use the average time-of-flight, or the median. Furthermore, it is important to note that the correct location to split the TPSF will depend on the thickness of the top layer

---

<sup>1</sup>This is not strictly true since it's possible that a photon took a long path and remained in the superficial layers. However, it is more likely that it, in fact, did reach a deeper layer than a photon with a short pathlength.

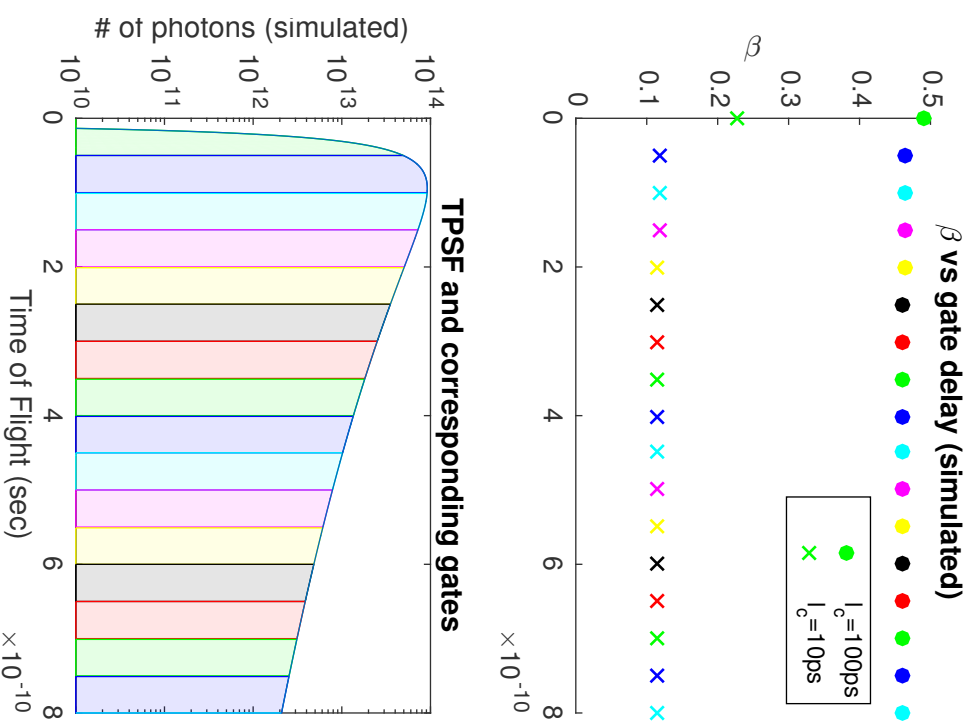
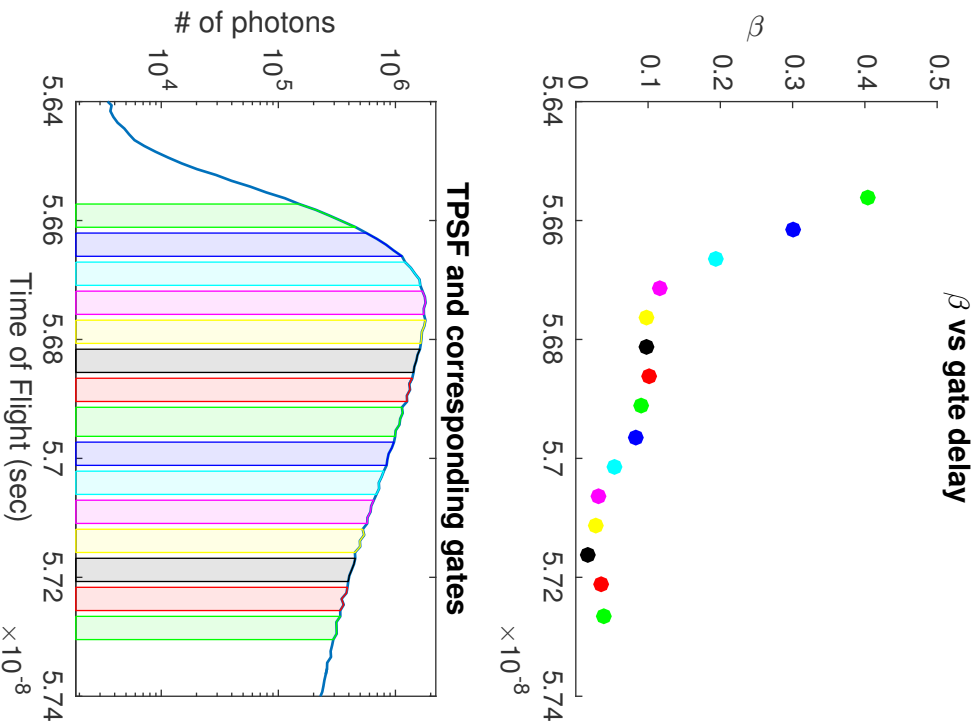


Figure 2.13: Effects on  $\beta$  of varying gate *delay* from (a) measurements and (b) simulations. All gates are 50ps wide and are shown as colored bars. Values of  $\beta$  are shown in corresponding colors.  $\rho = 10\text{mm}$ ,  $\mu_a = 0.51\text{cm}^{-1}$ ,  $\mu'_s = 5.67\text{cm}^{-1}$ .

and is unlikely to be in the “middle” by any of these metrics. A first approach may be to exhaustively split the TPSF at every plausible location, and recompute both the “early” and “late” autocorrelation functions and choose the splitting point to be the one that gives results most closely resembling those for each of the homogeneous media separately.

It is also necessary to consider the correlation diffusion model itself. It may be more appropriate to use a slab to model the propagation of “early” photons through the top layer, and a two-layer semi-infinite medium for the “late” photons. Note that if the absorption and scattering coefficients differ in the two layers, when computing the autocorrelation fit in the bottom layer it may not be fully appropriate to simply use the optical properties of the bottom layer – the photons reaching the bottom layer have already been scattered through the top layer and thus cannot be analyzed using the optical properties of the bottom layer alone. This question is further complicated for multi-layer models resembling biological systems of interest. The human head, for instance, has been modeled with up to 15 layers [67].

Another thing to consider regarding the correlation diffusion model is that the solution for  $G_1(\tau)$  (regardless of the geometry) assumes a continuous “source” of correlation that then diffuses and reaches a steady-state. For a continuous-wave light source, this model is intuitively satisfying since the light propagation also follows a steady-state diffusion solution. Further investigation into the validity of this assumption for a pulsed light source is necessary, as the correlation may in fact not diffuse according to a steady-state “correlation source” and there may be a drop in the autocorrelation function that is not accounted for by the finite coherence length model introduced by Bellini et. al. [55].

To model the effects of time-gating, we have modified the model from Bellini et. al. to instead consider subsets of the pathlength distribution. This model, however, does not fully account for our observations. To explain the mismatch between the predicted and measured

values of  $\beta$ , there are not only theoretical developments to consider but also practical. For instance, it may be necessary to look for artifacts in the laser pulse itself, as it may violate some of our assumptions. One such artifact is mode-hopping, where the laser switches longitudinal modes, resulting in discrete jumps in the wavelength [68] during operation. It is possible to address mode-hopping by operating at a lower power. Another is that the pulse may not be transform limited and the electric field may, for example, exhibit a “chirp” (i.e. the frequency of the electric field increases with time) during the pulse. In this case, transform limiting can be achieved by pulse compression. From a modeling perspective, if there is a chirp, the effective wavelength changes with varying gate delay, which is not considered for in the theoretical account given in §2.3.3.

Intermodal dispersion in the optical fibers may be yet another source of error due to instrumentation. If there is more than one propagation mode in the fiber (i.e. a multimode fiber), there will be broadening of the pulse since some rays will travel a shorter path through the fiber than others. While it can be neglected in CW operation, this broadening can be on the order of tens of picoseconds per meter, a significant portion of the pulse width itself. The impacts of this effect have so far been ignored in the analysis but need to be addressed. It is possible to reduce modal dispersion using a graded-index (GI) fiber to a few picoseconds per meter, or eliminate it using a single-mode fiber at the expense of light intensity.

To conclude, these have been only the first steps in constructing a clinically viable time-domain diffuse correlation spectroscopy system. We have constructed a first prototype and successfully demonstrated the viability of the method with initial measurements that produce reasonable estimates of Brownian diffusion in a phantom, compared to the measurements made by CW-DCS. We furthermore showed proof-of-concept with depth-resolved measurements in a two-layer phantom. We finally discussed the limitations of the current theoretical developments, which only partially explain the observations made using TD-DCS measure-

ments. Despite its early stages, this is undoubtedly an extremely promising technique for highly reliable measurements of blood flow and oxygenation, with a rich potential for biomedical optical imaging applications.

# Appendix A

## Code library

All code below is written in MATLAB 2015b. The most recent version, along with additional functions for visualization, can be found at <https://github.com/dtyulman/tddcs>.

### A.1 times\_to\_bins.m

```

1 function binned = times_to_bins(times, binWidth)
2 % Inputs:
3 % times: vector of photon arrival times, in units of the timer's
4 % resolution. Should only contain integers.
5 % binWidth: width of the bin, in units of the timer's resolution. Can be
6 % greater than zero if you want to oversample the times vector. Defaults
7 % to 1.
8
9 if nargin < 2
10     binWidth = 1;
11 end
12
13 times = times - times(1) + 1; %shift times s.t. first value is "1"
14 times = times/binWidth;
15 nBins = ceil( times(end) );
16 times = ceil(times);
17
18 binned = zeros(1, nBins);
19 for i = 1:length(times)
20     idx = times(i);
21     binned(idx) = binned(idx) + 1;
22 end
23
24 if binWidth > 1
25     binned = binned(1:end-1); %last bin might be invalid
26 end

```

## A.2 acorr\_times.m

```

1 function [acor, tau] = acorr_times(macro, maxLagTime, timerRes)
2 % Computes the autocorrelation directly from the photon arrival times
3
4 if nargin < 3
5     timerRes = 50e-9;
6 end
7 if nargin < 2
8     maxLagTime = 5e-3;
9 end
10
11 maxLag = ceil(maxLagTime/timerRes);
12 acor = zeros(1, maxLag);
13 diffs = diff(macro);
14 for i = 1:length(diffs)
15     j = 0;
16     cumulative = 0;
17     while i+j <= length(diffs) && cumulative+diffs(i+j) <= maxLag
18         cumulative = cumulative+diffs(i+j);
19         if cumulative > 0
20             acor(cumulative) = acor(cumulative)+1;
21         end
22         j = j + 1;
23     end
24 end
25
26 %Normalize
27 acor = acor * (macro(end)-macro(1)) / length(macro)^2;
28 tau = (1:length(acor))*timerRes;

```

## A.3 rebin\_to\_multitau.m

```

1 function [acorReb, tauReb] = rebin_to_multitau(acor, tau, nBins,
2     binFactor)
3
4 if nargin < 4
5     binFactor = 3; %factor by which binWidth increases after nBins
6     iterations
7 end
8 if nargin < 3
9     nBins = 30; %number of consecutive bins before increasing width
10 end
11
12 acorReb = [];
13 tauReb = [];

```

```

13 binWidth = 1; %starting bin width
14 binSum = 0;
15 ctr = 0;
16 binCtr = 0;
17 for i = 1:length(acor)
18     binSum = binSum + acor(i);
19     ctr = ctr + 1;
20     if ctr == binWidth
21         acorReb(end+1) = binSum/binWidth;
22         tauReb(end+1) = tau(i-floor(binWidth/2));
23         ctr = 0;
24         binSum = 0;
25         binCtr = binCtr+1;
26         if binCtr == nBins
27             binWidth = binWidth*binFactor;
28             binCtr = 0;
29         end
30     end
31 end

```

## A.4 dcs\_fit.m

```

1 function [beta, BFi] = dcs_fit(acorrdata, tau, muA, muSp, rho, wavlen,
   minTau, maxTau, plotName)
2 % Returns the beta and BFi values that provide the best fit of the DCS
   fit function to the measured autocorrelation data
3 %
4 % Inputs:
5 % acorrdata: measured autocorrelation data
6 % tau: lags for the autocorrelation data
7 % muA: absorption coefficient (cm-1)
8 % muSp: reduced scattering coefficient (cm-1)
9 % rho: source-detector separation (cm)
10 % wavlen: wavelength (nm)
11
12 if nargin > 6 && exist('minTau', 'var') && exist('maxTau', 'var')
13     [acorrdataFit, tauFit] = get_relevant_acorr_section(acorrdata, tau,
   minTau, maxTau);
14     piece = true;
15 else
16     [acorrdataFit, tauFit] = deal(acorrdata, tau);
17 end
18
19 init = [0.25, 1e-9]; %initial guess: [beta, BFi]
20 options = optimoptions(@lsqcurvefit, ...
21     'Algorithm', 'levenberg-marquardt', ...
22     'Display', 'off', ...
23     'ScaleProblem', 'jacobian');

```



```

24
25 fittedparams = lsqcurvefit(@(params, tau) dcs_fn(params, tau, muA, muSp,
    rho, wavlen), init, tauFit, acorrdataFit, [], [], options);
26 beta = fittedparams(1);
27 BFi = fittedparams(2);
28
29 if exist('plotName', 'var')
30     figure;
31     dcs_fit_plot(acorrdata, tau, beta, BFi, muA, muSp, rho, wavlen,
        plotName, minTau, maxTau)
32 end

```

## A.5 g2\_seminf.m

```

1 function g2 = g2_seminf(params, tau, muA, muSp, rho, wavelength, tau0)
2 % Normalized intensity autocorrelation for semi-infinite reflectance
   geometry
3 %
4 % Inputs:
5 % tau: lags (sec)
6 % mu_a: absorption coefficient (cm-1)
7 % mu_s: reduced scattering coefficient (cm-1)
8 % rho: source-detector separation (cm)
9 % wavelength (nm)
10
11 beta = params(1);
12 BFi = params(2);
13
14 C1 = 3*muSp*muA;
15 z0 = 1/(muSp + muA);
16 zb = 1.76/muSp;
17 k0 = (1.37*2*pi)/(wavelength*10^-7);
18 r1 = sqrt(rho^2 + z0^2);
19 r2 = sqrt(rho^2 + (z0 + 2*zb)^2);
20 C3 = 6*muSp^2*k0^2*BFi; % <- want to estimate BFi
21
22 if ~exist('tau0', 'var')
23     tau0 = tau(1);
24 end
25
26 A = exp(-r1*sqrt(C1 + C3*tau))/r1;
27 B = exp(-r2*sqrt(C1 + C3*tau))/r2;
28 C = exp(-r1*sqrt(C1 + C3*tau0))/r1;
29 D = exp(-r2*sqrt(C1 + C3*tau0))/r2;
30
31 g1 = (A - B) / (C - D);
32 g2 = 1 + beta*g1.^2; % <- want to estimate beta

```

## A.6 fold\_tpsf.m

```

1 function [countsFolded, tofFolded, shifts] = fold_tpsf(counts, tof,
    verbose)
2 % Inputs:
3 % counts - histogrammed "micro clock" photon counts
4 % tof - time of flight (micro clock values)
5 %
6 % Technically, the correct fold size is tpsfBins/(tofMax/pulsePeriod),
    but that's usually a non-integer so use autocorrelation to determine
    optimal fold size for each peak
7
8 if ~isrow(counts)
9     counts = counts';
10 end
11
12 %Find peak locations
13 acor=xcorr(counts, 'unbiased');
14 acor=acor(ceil(length(acor)/2):end);
15 [~, shifts] = findpeaks(acor, 'MinPeakProminence', acor(1)/4);
16
17 if verbose,
18     figure;
19     if exist('tof', 'var')
20         semilogy(tof, counts)
21     else
22         semilogy(counts)
23     end
24     title('Input')
25     figure;
26     subplot(1,2,1);
27     semilogy(counts); hold on;
28 end
29
30 %Fold based on autocorrelation peaks
31 countsFolded = counts;
32 for shift = shifts
33     countsFolded(1:end-shift) = countsFolded(1:end-shift) +
        counts(1+shift:end);
34     if verbose
35         semilogy(counts(1+shift:end));
36     end
37 end
38
39 %Return only the first peak onto which all others were folded
40 first = find(counts>0, 1);
41 minFoldLength = min(diff( [0, shifts, length(counts)] ));
42 last = first + minFoldLength;
43 countsFolded = countsFolded(first:last);
44

```

```

45 if verbose
46     xlim([first,last]);
47     subplot(1,2,2);
48     semilogy(countsFolded);
49 end
50
51
52 %Return relevant time of flight information, if needed
53 if nargin > 1
54     if nargin < 2
55         error('Must provide time of flight as second argument')
56     end
57     tofFolded = tof(first:last);
58
59     if verbose
60         figure;
61         semilogy(tofFolded, countsFolded);
62         title('Folded')
63     end
64 end

```

## A.7 fold\_micro.m

```

1 function [microFolded, countsFolded, tofFolded] = fold_micro(micro,
2     microRes, verbose)
3 % Performs the TPSF folding operation on the micro clock values rather
4 %   than the histogrammed photon counts (see also fold_tpsf)
5 % Inputs:
6 %   micro = micro clock time
7 %   maxTof = longest time of flight when recording the TPSF, in
8 %   nanoseconds. Defaults to 50
9 %   tpsfBins = number of time bins used when recording the TPSF. Defaults
10 %   to 4096
11
12 if nargin < 3
13     verbose = false;
14 end
15
16 %Histogram the micro clock values
17 [counts, tofIdx] = histcounts(micro, 0:max(micro));
18 tof = tofIdx(1:end-1)*microRes;
19
20 %Fold histogrammed values to get shifts
21 [countsFolded, tofFolded, shifts] = fold_tpsf(counts, tof, verbose);
22
23 %Shift the micro clock values
24 microFolded = micro;
25 for shift = shifts

```

```

22     foldIdxs = (micro >= shift);
23     microFolded(foldIdxs) = micro(foldIdxs) - shift;
24 end

```

## A.8 g2\_sim.m

```

1 function [g2, taus] = g2sim(params, taus, tmin, tmax)
2
3 % ----- parse inputs -----
4 if ~exist('tmin', 'var') || isempty(tmin)
5     tmin = 0;
6 end
7 if ~exist('tmax', 'var') || isempty(tmax)
8     tmax = 5e-9;
9 end
10 if ~exist('taus', 'var') || isempty(taus)
11     taus = [0 logspace(-7, 0, 100)];
12 end
13
14 muA = params.muA; %absorption coeff (1/mm)
15 muSp = params.muSp; %scattering coeff (1/mm)
16 rho = params.rho; %source-detector separation (mm)
17 Db = params.Db; %Brownian diffusion coeff (i.e. BFi) (Note: doesn't
    affect beta)
18 if isfield(params, 'n')
19     n = params.n; %index of refraction
20 else
21     n = 1.33; %defaults to water
22 end
23 v = 3e11 / n; %speed of light in medium (mm/sec)
24 if isfield(params, 'pulseWidth')
25     tCoh = params.pulseWidth; %(sec) assuming transform limited,
        [coherence time]=[pulse width]
26     lCoh = v*tCoh; %coherence length (mm)
27 elseif isfield(params, 'lCoh')
28     lCoh = params.lCoh;
29 end
30 lambda = params.lambda; %laser wavelength (mm)
31 ko = 2*pi*n/lambda;
32
33 % ----- TPSF integrand -----
34 TPSF = @(t) TPSFsim(t, muA, muSp, rho, n);
35 TPSFnorm = integral(TPSF,tmin,tmax);
36
37 % ----- g2 integrand -----
38 P = @(t) TPSF(t) / TPSFnorm; %pathlength distribution
39 g1 = @(t, tau) exp( - v*t*muSp * ko^2 * 2*Db*tau );
40 g2integrandTau = @(t1, t2, tau) ... %Bellini Eq.7

```

```

41     P(t1) .* P(t2) .* g1(t1, tau) .* g1(t2, tau) .* exp(
        -2*(v*(t1-t2)/lCoh).^2 );
42
43 % ----- Calculate g2 for every tau -----
44 g2 = nan(size(taus));
45 for i = 1:length(taus)
46     tau = taus(i);
47     g2integrand = @(t1, t2) g2integrandTau(t1, t2, tau);
48     g2(i) = 1 + integral2(g2integrand,tmin,tmax,tmin,tmax);
49 end

```

## A.9 tpsf\_sim.m

```

1 function tpsf = tpsf_sim(t, muA, muSp, rho, n)
2 %TPSF for semi-infinite reflection geometry
3
4 v = 3e11 / n; %speed of light in medium (mm/sec)
5 D = v/(3*muSp);
6 R = -1.440./n^2+0.710/n+0.668+0.0636*n; % Effective reflection coefficient
7 ze = 2/3*(1+R)/(1-R); % Extrapolated boundary is given by ze divided by
    musp
8 r1 = sqrt( rho^2 + 1/muSp^2 );
9 r2 = sqrt( rho^2 + (1+2*ze)^2/muSp^2 );
10
11 tpsf = t.^(-3/2) .* exp(-v*muA*t) .* (exp( -r1^2./(4*D*t) ) - exp(
    -r2^2./(4*D*t) ) );

```

## References

- [1] D. A. Boas, C. E. Elwell, M. Ferrari, and G. Taga, "Twenty years of functional near-infrared spectroscopy: introduction for the special issue," *NeuroImage*, vol. 85, 2014. DOI: 10.1016/j.neuroimage.2013.11.033.
- [2] F. Scholkmann, S. Kleiser, A. J. Metz, R. Zimmermann, J. Mata Pavia, U. Wolf, and M. Wolf, "A review on continuous wave functional near-infrared spectroscopy and imaging instrumentation and methodology," *NeuroImage*, vol. 85, Jan. 2014. DOI: 10.1016/j.neuroimage.2013.05.004.
- [3] A. Sakudo, "Near-infrared spectroscopy for medical applications: current status and future perspectives," *Clinica Chimica Acta*, vol. 455, no. February, 2016. DOI: 10.1016/j.cca.2016.02.009.
- [4] T. Durduran and A. G. Yodh, "Diffuse correlation spectroscopy for non-invasive, micro-vascular cerebral blood flow measurement.," *NeuroImage*, vol. 85 Pt 1, no. Durduran, T., & Yodh, A. G. (2014). *NeuroImage* Diffuse correlation spectroscopy for non-invasive , micro-vascular cerebral blood flow measurement. *NeuroImage*, 85, 5163. <http://doi.org/10.1016/j.neuroimage.2013.06.017>, Jan. 2014. DOI: 10.1016/j.neuroimage.2013.06.017.
- [5] E. M. Buckley, A. B. Parthasarathy, P. E. Grant, A. G. Yodh, and M. A. Franceschini, "Diffuse correlation spectroscopy for measurement of cerebral blood flow: future prospects.," *NeuroPhotonics*, vol. 1, no. 1, 2014. DOI: 10.1117/1.NPh.1.1.011009.
- [6] T. Durduran, R. Choe, W. B. Baker, and A. G. Yodh, "Diffuse optics for tissue monitoring and tomography," *Reports on Progress in Physics*, vol. 73, no. 7, 2010. DOI: 10.1088/0034-4885/73/7/076701.
- [7] P.-Y. Lin, N. Roche-Labarbe, M. Dehaes, S. Carp, A. Fenoglio, B. Barbieri, K. Hagan, P. E. Grant, and M. A. Franceschini, "Non-invasive optical measurement of cerebral metabolism and hemodynamics in infants.," *Journal of Visualized Experiments*, no. March, 2013. DOI: 10.3791/4379.
- [8] G. Strangman, D. A. Boas, and J. P. Sutton, "Non-invasive neuroimaging using near-infrared light," *Biological Psychiatry*, vol. 52, no. 7, 2002. DOI: 10.1016/S0006-3223(02)01550-0.

- [9] J. Selb, J. J. Stott, M. A. Franceschini, A. G. Sorensen, and D. A. Boas, "Improved sensitivity to cerebral hemodynamics during brain activation with a time-gated optical system: analytical model and experimental validation.," *Journal of biomedical optics*, vol. 10, no. 1, 2005. DOI: 10.1117/1.1852553.
- [10] F. Scholkmann and M. Wolf, "General equation for the differential pathlength factor of the frontal human head depending on wavelength and age," *Journal of biomedical optics*, vol. 18, no. 10, 2013. DOI: 10.1117/1.JBO.18.10.105004.
- [11] M. Wolf, M. Ferrari, and V. Quaresima, "Progress of near-infrared spectroscopy and topography for brain and muscle clinical applications.," *Journal of biomedical optics*, vol. 12, no. 6, 2007. DOI: 10.1117/1.2804899.
- [12] F. Jobsis, "Noninvasive, infrared monitoring of cerebral and myocardial oxygen sufficiency and circulatory parameters," *Science*, vol. 198, no. 4323, Dec. 1977. DOI: 10.1126/science.929199.
- [13] M. Ferrari and V. Quaresima, "A brief review on the history of human functional near-infrared spectroscopy (fnirs) development and fields of application.," *NeuroImage*, vol. 63, no. 2, Nov. 2012. DOI: 10.1016/j.neuroimage.2012.03.049.
- [14] D. A. Boas, C. Pitris, and N. Ramanujam, Eds., *Handbook of biomedical optics*. Boca Raton, FL : CRC Press, c2011., 2011, ISBN: 1420090372.
- [15] S. J. Madsen, Ed., *Optical methods and instrumentation in brain imaging and therapy*. Ser. Bioanalysis. New York, NY : Springer, c2013., 2013, ISBN: 9781461449782.
- [16] M. A. O'Leary, "Imaging with diffuse photon density waves," PhD thesis, University of Pennsylvania, 1996. [Online]. Available: <http://repository.upenn.edu/dissertations/AAI9712984/>.
- [17] V. Ntziachristos, "Going deeper than microscopy: the optical imaging frontier in biology.," *Nature methods*, vol. 7, no. 8, 2010. DOI: 10.1038/nmeth.1483.
- [18] D. A. Boas, J. P. Culver, J. J. Stott, and A. Dunn, "Three dimensional monte carlo code for photon migration through complex heterogeneous media including the adult human head," *Optics Express*, vol. 10, no. 3, 2002.
- [19] M. S. Patterson, B. Chance, and B. Wilson, "Time resolved reflectance and transmittance for the non-invasive measurement of tissue optical properties," *Applied Optics*, vol. 28, no. 12, 1989. DOI: 10.1364/AO.28.002331.
- [20] T. J. Farrell, M. S. Patterson, and B. Wilson, "A diffusion theory model of spatially resolved, steady-state diffuse reflectance for the noninvasive determination of tissue optical properties in vivo," *Medical Physics*, vol. 19, no. 4, Jul. 1992. DOI: 10.1118/1.596777.

- [21] S. Fantini, M. A. Franceschini, and E. Gratton, "Semi-infinite-geometry boundary problem for light migration in highly scattering media: a frequency-domain study in the diffusion approximation," *Journal of the Optical Society of America B*, vol. 11, no. 10, 1994. DOI: 10.1364/JOSAB.11.002128.
- [22] A. Kienle and M. S. Patterson, "Improved solutions of the steady-state and the time-resolved diffusion equations for reflectance from a semi-infinite turbid medium.," *Journal of the Optical Society of America A*, vol. 14, no. 1, Jan. 1997. DOI: 10.1364/JOSAA.14.000246.
- [23] D. T. Delpy, M. Cope, P. van der Zee, S. R. Arridge, S. Wray, and J. Wyatt, "Estimation of optical pathlength through tissue from direct time of flight measurement.," *Physics in medicine and biology*, vol. 33, no. 12, 1988. DOI: 10.1088/0031-9155/33/12/008.
- [24] B. Chance, J. S. Leigh, H. Miyake, D. S. Smith, S. Nioka, R. Greenfeld, M. Finander, K. Kaufmann, W. Levy, and M. Young, "Comparison of time-resolved and -unresolved measurements of deoxyhemoglobin in brain.," *Proceedings of the National Academy of Sciences*, vol. 85, no. 14, 1988. DOI: 10.1073/pnas.85.14.4971.
- [25] M. A. Franceschini, E. Gratton, and S. Fantini, "Noninvasive optical method of measuring tissue and arterial saturation: an application to absolute pulse oximetry of the brain.," *Optics letters*, vol. 24, no. 12, Jun. 1999. DOI: 10.1364/OL.24.000829.
- [26] D. T. Delpy and M. Cope, "Quantification in tissue near-infrared spectroscopy," *Philosophical Transactions of the Royal Society B: Biological Sciences*, vol. 352, no. 1354, Jun. 1997. DOI: 10.1098/rstb.1997.0046.
- [27] J. B. Fishkin and E. Gratton, "Propagation of photon-density waves in strongly scattering media containing an absorbing semi-infinite plane bounded by a straight edge.," *Journal of the Optical Society of America A*, vol. 10, no. 1, 1993. DOI: 10.1364/JOSAA.10.000127.
- [28] D. A. Boas, "Diffuse photon probes of structural and dynamical properties of turbid media: theory and biomedical applications," PhD thesis, University of Pennsylvania, 1996. [Online]. Available: <http://repository.upenn.edu/dissertations/AAI9636132/>.
- [29] A. Torricelli, D. Contini, A. Pifferi, M. Caffini, R. Re, L. Zucchelli, and L. Spinelli, "Time domain functional nirs imaging for human brain mapping," *NeuroImage*, vol. 85, 2014. DOI: 10.1016/j.neuroimage.2013.05.106.
- [30] M. Wahl, "Time-correlated single photon counting," Tech. Rep., 2014. DOI: 10.1016/0022-2313(89)90051-3.
- [31] W. Becker, *Advanced time-correlated single photon counting techniques*. Ser. Springer series in chemical physics: 81. Berlin ; New York : Springer, c2005., 2005, ISBN: 3540260471.
- [32] W. Becker, *The bh TCSPC Handbook, Sixth Edition*. 2014. [Online]. Available: <http://www.becker-hickl.de/handbook.htm>.



- [33] E. Hecht, *Optics*. Reading, Mass. : Addison-Wesley, c2002., 2002, ISBN: 0805385665.
- [34] K. S. Schmitz, *An introduction to dynamic light scattering of macromolecules*. Academic Press., 1990, ISBN: 978-0-12-627260-4.
- [35] R. Pecora, *Dynamic light scattering : Applications of photon correlation spectroscopy*. New York : Plenum Press, c1985., 1985, ISBN: 0306417901.
- [36] B. J. Berne and R. Pecora, *Dynamic light scattering: With applications to chemistry, biology, and physics*. New York : Wiley, c1976., 1976, ISBN: 0471071005.
- [37] W. Brown, Ed., *Dynamic light scattering: The method and some applications*. Ser. Monographs on the physics and chemistry of materials: 49. Oxford [England] : Clarendon Press ; New York : Oxford University Press, 1993., 1993, ISBN: 0198539428.
- [38] “Static light scattering technologies for GPC/SEC explained,” Malvern Instruments Limited, Worcestershire, UK, Tech. Rep., 2013.
- [39] J. D. Briers, “Laser doppler, speckle and related techniques for blood perfusion mapping and imaging,” *Physiological Measurement*, vol. 22, no. 4, R35–R66, Nov. 2001. DOI: 10.1088/0967-3334/22/4/201.
- [40] A. J. F. Siegert, “On the fluctuations in signals returned by many independently moving scatterers,” Tech. Rep., 1943.
- [41] D. A. Boas and A. G. Yodh, “Spatially varying dynamical properties of turbid media probed with diffusing temporal light correlation,” *Journal of the Optical Society of America A*, vol. 14, no. 1, 1997. DOI: 10.1364/JOSAA.14.000192.
- [42] M. Ninck, M. Untenberger, and T. Gisler, “Diffusing-wave spectroscopy with dynamic contrast variation: disentangling the effects of blood flow and extravascular tissue shearing on signals from deep tissue,” *Biomedical optics express*, vol. 1, no. 5, 2010. DOI: 10.1364/BOE.1.001502.
- [43] G. Maret and P. E. Wolf, “Multiple light scattering from disordered media. the effect of brownian motion of scatterers,” *Zeitschrift fur Physik B Condensed Matter*, vol. 65, no. 4, Jul. 1986. DOI: 10.1007/BF01303762.
- [44] A. G. Yodh, P. D. Kaplan, and D. J. Pine, “Pulsed diffusive-wave spectroscopy: high resolution through nonlinear optical gating,” *Physical Review B*, vol. 42, no. 7, Sep. 1990. DOI: 10.1103/PhysRevB.42.4744.
- [45] D. J. Pine, D. A. Weitz, J. Zhu, and E. Herbolzheimer, “Diffusing-wave spectroscopy: dynamic light scattering in the multiple scattering limit,” *Journal de Physique*, vol. 51, no. 18, 1990. DOI: 10.1051/jphys:0199000510180210100.
- [46] C. Cheung, J. P. Culver, K. Takahashi, J. H. Greenberg, A. G. Yodh, E. Luzia, and D. E. S. Santos, “In vivo cerebrovascular measurement combining diffuse near-infrared absorption and correlation spectroscopies,” *Physics in Medicine and Biology*, vol. 46, no. 8, 2001. DOI: 10.1088/0031-9155/46/8/302.

- [47] B. J. Ackerson, R. L. Dougherty, N. M. Reguigui, and U. Nobbmann, "Correlation transfer - application of radiative transfer solution methods to photon correlation problems," *Journal of Thermophysics and Heat Transfer*, vol. 6, no. 4, Oct. 1992. DOI: 10.2514/3.11537.
- [48] R. L. Dougherty, B. J. Ackerson, N. M. Reguigui, F. Dorri-Nowkooorani, and U. Nobbmann, "Correlation transfer: development and application," *Journal of Quantitative Spectroscopy and Radiative Transfer*, vol. 52, no. 6, 1994. DOI: 10.1016/0022-4073(94)90037-X.
- [49] D. A. Boas, L. E. Campbell, and A. G. Yodh, "Scattering and imaging with diffusing temporal field correlations," *Physical Review Letters*, vol. 75, no. 9, Aug. 1995. DOI: 10.1103/PhysRevLett.75.1855.
- [50] J. Rička, "Dynamic light scattering with single-mode and multimode receivers.," *Applied optics*, vol. 32, no. 15, May 1993. DOI: 10.1364/AO.32.002860.
- [51] E. Van Keuren, H. Wiese, and D. Horn, "Diffusing-wave spectroscopy in concentrated latex dispersions: an investigation using single-mode fibers," *Colloids and Surfaces A: Physicochemical and Engineering Aspects*, vol. 77, no. 1, Sep. 1993. DOI: 10.1016/0927-7757(93)80096-W.
- [52] D. Irwin, L. Dong, Y. Shang, R. Cheng, M. Kudrimoti, S. D. Stevens, and G. Yu, "Influences of tissue absorption and scattering on diffuse correlation spectroscopy blood flow measurements.," *Biomedical optics express*, vol. 2, no. 7, 2011. DOI: 10.1364/BOE.2.001969.
- [53] J. Sutin, M. A. Franceschini, D. A. Boas, and J. Selb, "Systems and methods for time-resolved diffuse correlation spectroscopy," 62/145,104, 2015. [Online]. Available: <https://www.google.com/patents/WO2016164900A1>.
- [54] J. Sutin, B. Zimmerman, D. Tyulmankov, D. Tamborini, K. C. Wu, J. Selb, A. Gulinatti, I. Rech, A. Tosi, D. A. Boas, and M. A. Franceschini, "Time-domain diffuse correlation spectroscopy," *Optica*, vol. 3, no. 9, 2016. DOI: 10.1364/OPTICA.3.001006.
- [55] T. Bellini, M. A. Glaser, N. A. Clark, and V. Degiorgio, "Effects of finite laser coherence in quasielastic multiple scattering," *Physical Review A*, vol. 44, no. 8, 1991. DOI: 10.1103/PhysRevA.44.5215.
- [56] A. Gulinatti, I. Rech, F. Panzeri, C. Cammi, P. Maccagnani, M. Ghioni, and S. Cova, "New silicon spad technology for enhanced red-sensitivity, high-resolution timing and system integration," *Journal of Modern Optics*, vol. 59, no. 17, 2012. DOI: 10.1080/09500340.2012.701340.
- [57] A. Giudice, G. Simmerle, D. Veronese, R. Biasi, A. Gulinatti, I. Rech, M. Ghioni, and P. Maccagnani, "High-detection efficiency and picosecond timing compact detector modules with red-enhanced spads," May 2012. DOI: 10.1117/12.919120.

- [58] J. C. B. Kangara, A. J. Hachtel, M. C. Gillette, J. T. Barkeloo, E. R. Clements, S. Bali, B. E. Unks, N. A. Proite, D. D. Yavuz, P. J. Martin, J. J. Thorn, and D. A. Steck, "Design and construction of cost-effective tapered amplifier systems for laser cooling and trapping experiments," *American Journal of Physics*, vol. 82, no. 8, Aug. 2014. DOI: 10.1119/1.4867376.
- [59] M. Poelker, "High power gain-switched diode laser master oscillator and amplifier," *Applied Physics Letters*, vol. 67, no. 19, Nov. 1995. DOI: 10.1063/1.114585.
- [60] A. V. Oppenheim, A. S. Willsky, and S. H. Nawab, *Signals & Systems*. Ser. Prentice-Hall signal processing series. Upper Saddle River, N.J. : Prentice Hall, c1997., 1997, ISBN: 0138147574.
- [61] T. H. Cormen, C. E. Leiserson, R. L. Rivest, and C. Stein, *Introduction to algorithms*. Cambridge, Mass. : MIT Press, c2009., 2009, ISBN: 9780262033848.
- [62] D. Magatti and F. Ferri, "Fast multi-tau real-time software correlator for dynamic light scattering," *Applied Optics*, vol. 40, no. 24, Aug. 2001. DOI: 10.1364/AO.40.004011.
- [63] *ISS MetaOx Tissue Oxygen Consumption Monitor*. [Online]. Available: <http://www.iss.com/biomedical/instruments/metaox.html>.
- [64] J. J. Moré, "The levenberg-marquardt algorithm: implementation and theory," in *Lecture Notes in Mathematics*, vol. 630, 1978. DOI: 10.1007/BFb0067700.
- [65] M. Zhao, L. Jin, B. Chen, Y. Ding, D. Chen, and H. Ma, "Afterpulsing and its correction in fluorescence correlation spectroscopy experiments.," *Applied optics*, vol. 42, no. 19, 2003. DOI: 0003-6935/03/194031-06.
- [66] S. Prahl, *Mie scattering calculator*, 2012. [Online]. Available: [http://omlc.org/calc/mie\\_calc.html](http://omlc.org/calc/mie_calc.html) (visited on 01/01/2017).
- [67] J. Steinbrink, H. Wabnitz, H. Obrig, A. Villringer, and H. Rinneberg, "Determining changes in nir absorption using a layered model of the human head.," *Physics in medicine and biology*, vol. 46, no. 3, 2001. DOI: 10.1088/0031-9155/46/3/320.
- [68] T. A. Heumier, "Mode hopping in semiconductor lasers," PhD thesis, Dept. of Physics, Montana State University, 1992. [Online]. Available: <http://scholarworks.montana.edu/xmlui/handle/1/7215>.